AN EVALUATION OF NEUTRAL AND CONVECTIVE PLANETARY BOUNDARY-LAYER PARAMETERIZATIONS RELATIVE TO LARGE EDDY SIMULATIONS

KEITH W. AYOTTE, PETER P. SULLIVAN, ANDERS ANDRÉN, SCOTT C. DONEY, ALBERT A. M. HOLTSLAG, WILLIAM G. LARGE, JAMES C. MCWILLIAMS, CHIN-HOH MOENG, MARTIN J. OTTE, JOSEPH J. TRIBBIA and JOHN C. WYNGAARD

Mesoscale and Microscale Meteorology Division, National Center for Atmospheric Research, P.O. Box 3000, Boulder, Colorado, 80307-3000, U.S.A.

(Received in final form 5 December, 1995)

Abstract. This paper compares a number of one-dimensional closure models for the planetary boundary layer (PBL) that are currently in use in large-scale atmospheric models. Using the results of a large-eddy simulation (LES) model as the standard of comparison, the PBL models are evaluated over a range of stratifications from free convective to neutral and a range of surface shear stresses. Capping inversion strengths for the convective cases range from weakly to strongly capped. Six prototypical PBL models are evaluated in this study, which focuses on the accuracy of the boundary-layer fluxes of momentum, heat, and two passive scalars. One scalar mimics humidity and the other is a top-down scalar entrained into the boundary layer from above. A set of measures based on the layer-averaged differences of these fluxes from the LES solutions is developed. In addition to the methodological framework and suite of LES solutions, the main result of the evaluation is the recognition that all of the examined PBL parameterizations have difficulty reproducing the entrainment at the top of the PBL, as given by the LES, in most parameter regimes. Some of the PBL models are relatively accurate in their entrainment flux in a subset of parameter regimes. The sensitivity of the PBL models to vertical resolution is explored, and substantive differences are observed in the performance of the PBL models, relative to LES, at low resolution typical of large scale atmospheric models.

Key words: closure, large-eddy simulation, comparison, turbulent

1. Introduction

It seems clear that with the computational capabilities available even in the foreseeable future, modelling of the atmosphere or the atmosphere/ocean system will not be carried out at vertical and horizontal resolutions sufficient to resolve eddies responsible for turbulent transport of heat, mass and momentum. Therefore it seems reasonable to assume that large-scale models will continue to require some form of parameterization of turbulent processes. As pointed out in a review of the role of planetary boundary layer (PBL) models within climate models by Brown and Foster (1994), the role of turbulent transport appears crucial. Given the importance of turbulent transport and its modelling within climate and large scale models, it is reasonable to examine the sensitivity of climate simulations to these parameterizations. Towards that end, this work attempts to quantify the ability of a number of boundary-layer schemes to represent turbulent transfer within the PBL.

Boundary-Layer Meteorology **79:** 131–175, 1996.

Table I
Results of model survey.

GCM	Total levels	PBL Levels	Closure
BMRC	9	2	K(R_i)
Canadian Climate Centre	15	2–3	K(R_i)
ECMWF	19	4	K(R_i)
GFDL-Manabe	30	6	K(R_i)-MY-2.5
GFDL-Miyakoda	18	4	K(R_i)-MY-2.5
GLA	17	2–3	MY-2.5
Los Alamos	20	$\Delta z_s = 30$m	K(R_i)
NCAR-CCM1	12	1	K(R_i)
NMC-MRF		3–4	K(R_i)
NMC-eta		$\Delta z_s = 30$mb	$K(R_i)$-MY-2.5
NMC-NGM	16	5	N. Phillips
Oregon State		$\Delta z_s = 20 - 50$m	K-profile
U.K. Meteorological Office		2	K(R_i)
U. Hamburg	19	4	$K(R_i)$
U. Maryland	18	3–4	$K(R_i)$
UCLA-CSU		1	mixed-layer model

This investigation has its origins in the Planetary Boundary Layer Model Workshop which was part of The World Climate Research Programme held at the European Centre for Medium-Range Forecasts in 1989 (Taylor and Wyngaard, 1990). As part of this workshop, a survey of twenty climate research groups was conducted; sixteen of these responded. Table I gives a list of the closures used within global climate models (GCMs) along with the total number of model levels within the boundary layer. The survey indicated that the closures fell into a few broad categories. Most research groups use some form of a K(R_i) scheme (i.e., a stability-dependent eddy diffusivity), with the Mellor and Yamada (1974, 1982) level 2.5 also in use. In addition, the survey showed groups using the K-profile scheme (Troen and Mahrt, 1986), and the mixed-layer model (Tennekes and Driedonks, 1981 and Driedonks, 1982).

In an effort to make our comparison of broader interest, it has not been restricted to closures found in climate models. Closures used in forecast and mesoscale models have also been included so that their potential for use in climate models can be evaluated. Based on this reasoning and the above survey, Table II shows a number of general categories of turbulence closure chosen for our evaluation.

In a review on the sensitivity of climate simulations to land-surface and boundary-layer treatments, Garratt (1993) emphasized the need for intercomparisons of PBL models both in isolation and within GCMs. In general, evaluations of boundary-layer schemes tend to be of a few different types. One is comparison of GCM results using boundary-layer treatments that vary between runs. This type of study has been

Table II
Generic Model Categories.

Model Type	Authors
$K(Ri)$	(Louis, 1979, Louis, Tiedtke and Geleyn, 1981)
single-point	(Mellor and Yamada, 1974, 1982)
K-profile	(Troen and Mahrt, 1986, Holtslag *et al.*, 1990, and Holtslag and Boville, 1993)
mixed-layer	(Tennekes and Driedonks, 1981 and Driedonks, 1982)
stability-bounds	(Price and Weller, 1986)
multi-stream exchange	(Stull, 1984, 1993)

undertaken recently by Holtslag and Boville (1993) with the NCAR CCM2 model. They compared model results from a $K(Ri)$ scheme with those from an updated K-profile scheme, assessing the impact on the climate simulation. Garratt (1993) cites a number of other such sensitivity studies, which can reveal sensitivities of the large-scale model that may be the result of interaction between many complex, non-linear systems within the model. This can also be a disadvantage in that the complexity of the interactions may very well obscure the behaviour of the PBL treatment.

Another type of examination involves the comparison of PBL model results with atmospheric measurements, most often using a profile version of the model. For example, Andrén (1990) compared mean and turbulent quantities with measurements from a stratocumulus-topped marine boundary layer (Brost *et al.*, 1982) and from the KONTUR PBL experiment (Grant, 1986). Betts and Miller (1986) used GATE (Thompson *et al.*, 1979), BOMEX (Holland and Rasmusson, 1973), ATEX (Augstein *et al.*, 1973) and arctic air-mass data sets to evaluate transport and convection parameterization schemes. Similarly, Yamada and Mellor (1979) use BOMEX data to examine the performance of a second-order turbulence closure coupled with an ensemble cloud model. Yamada and Mellor (1975) used the Wangara data set (Clarke *et al.*, 1971) to examine the behaviour of the level-3 version of the Mellor and Yamada (1974, 1982) second-order-closure model through several diurnal cycles during days 33-35 of the experiment. In such comparisons a number of assumptions and interpolations are typically required to match the data with the model forcing parameters. Interpolations and smoothing are also often required to transform observational data so that comparison is possible. This is seldom a straightforward undertaking, but one advantage of such studies is clearly the link with the real atmosphere.

Ideally, the benchmark for evaluating PBL models would be measurements of the full set of variables to be modelled over the entire parameter space in which the models are intended to operate. Unfortunately, there still exists the "*fact gap*" that Bradshaw (1972) referred to more than two decades ago. This fact gap was created

as the computational power available for running turbulence models began to far exceed the available data base on turbulent flows. These data-base limitations stem from the inherent difficulty of measuring turbulent flows, as discussed by Corrsin (1963). Three of the limiting difficulties are the imperfect response of sensors, the inability to measure full, three-dimensional properties in general (and the inability to measure certain turbulence properties at all), and the need for long averaging times to generate reliable statistics. These problems are particularly severe in atmospheric turbulence (Lenschow, 1986). Atmospheric measurements tend also to suffer from changing ambient conditions and departures between the underlying flows and our idealizations of them. As a result, Bradshaw's "fact gap" is particularly prominent in atmospheric turbulence.

For this reason, developers of turbulence closures often augment their data base with turbulence simulations (see, for example, Randall *et al.*, 1992; Moeng and Wyngaard, 1989; Deardorff, 1972a.) In this study we have used large-eddy simulation (LES) to help evaluate the behaviour of a number of turbulence closures. The simulations are of a series of PBLs ranging from neutral to strongly convective. This method has the advantage that within a limited parameter space, we are free to vary a number of model parameters such as surface heating, mean thermodynamic structure, and the geostrophic wind profile. In addition, scalars can be introduced into the model domain using mean concentration distributions that facilitate the detailed study of turbulent transport. Also of advantage is the ability to extract any of the model variables at any time during the simulation at any point within the model domain.

Examination of closures for pressure covariance, higher order moments and molecular destruction is particularly suited to comparison with LES output as is demonstrated by Moeng and Wyngaard (1989). The approach here is to some extent different in that it focuses on the overall behaviour of methods designed to encompass all of these processes. This makes the task of evaluation more difficult as we are examining the behaviour of a coupled nonlinear system rather than isolated aspects of any particular closure. It also makes performance measures difficult to define. This has lead to modelling in a restricted parameter space in part due to the above difficulties and in part due to the desire to define and quantify first the simpler characteristics of the closures before moving onto more complex situations. The comparison does show the performance of the schemes in modelling very simple types of atmospheric boundary layers. In so doing, the comparison suggests standards for what might be considered necessary but not sufficient performance. The study also demonstrates a number of measures that can be used to assess the ability of the closures to model vertical turbulent transfer in a large-scale model. The subset of cases presented here can be considered a starting point for further comparisons and evaluations. These might include the stable PBL, PBLs including moist convection, or PBLs interacting with irregular terrain.

In the next section we provide a context in which we can qualify the comparisons to be made and describe the parameters and methods used to carry out

the simulations. The section following is a general overview of the modelling framework and boundary conditions used in the comparison. We then describe the modelling experiments and integration sequence used to derive the profiles used as a basis for comparison of the LES and the PBL model results. Section 6 presents a number of measures used to assess the model performance and presents the results of the comparisons. The final section concludes with an overview of the model performance. Detailed model descriptions are presented in Appendix A.

2. A Basis for Comparison

LES originated with Deardorff (1970, 1972a) and now finds extensive use in both geophysical and engineering studies (for reviews see Rogallo and Moin, 1984; Galperin and Orszag, 1993). LES separates the flow field into two components: a large-eddy (or resolvable-scale) field and a residual (or subgrid-scale) field. The philosophy behind this division is that large scales in a turbulent flow contain most of the energy and flux and therefore are of prime importance. Moreover the resolved field is more dependent on boundary conditions and thus varies markedly depending on the physical situation modelled. On the other hand, the small-scale motions contain appreciably less energy and are more isotropic and universal in their behaviour. Thus, a model that resolves the large-scale turbulent motions and parameterizes the rest can be expected to exhibit some generality and possess reasonable predictive capabilities.

LES provides time-dependent, three-dimensional fields of velocity, pressure, temperature, and advected scalars subject to a wide variety of boundary-layer forcing. Furthermore, with LES it is possible to simulate realistic flow conditions in a controlled fashion. For example, buoyancy, geostrophic wind, capping-inversion strength, surface boundary conditions, and surface roughness can be readily modified in LES. Each LES integration serves as an "experiment" in its own right, and provides a complement to direct measurements.

LES is maturing to a stage where it is giving us insight into atmospheric boundary-layer properties that have been measured only poorly, if at all. LES results outstrip oceanic observations enormously. A recent comparison of several planetary boundary-layer LES codes revealed that despite the differences in numerical methods and subgrid-scale modelling, the code-to-code variation in results was less than the scatter in the available experimental data (Nieuwstadt *et al.*, 1993; Andrén *et al.*, 1994). It can also be noted here that LES does predict a number of the salient features of the convective boundary layer. These include the ratio of surface to entrainment flux in the free convective limit and second moment profiles from convective boundary layers in laboratory experiments and from the atmosphere (Nieuwstadt *et al.*, 1993). However, it still must be noted that there remains a degree of uncertainty in LES results in light of our inability to accurately measure many quantities in the convective atmospheric boundary layer.

The LES code that forms the basis of our study was developed by Moeng (1984), and has been used in numerous studies of the PBL. For example, Moeng and Wyngaard (1989) studied convection dominated PBLs, McWilliams *et al.* (1991) investigated shear driven oceanic PBLs, and Moeng and Schumann (1991) examined stratus-topped PBLs.

3. The LES Database

3.1. The LES Code

The LES code used in the PBL evaluation solves the filtered Navier-Stokes equations using a mixed finite difference, pseudo-spectral method. Derivatives in the $x - y$ plane are evaluated pseudo-spectrally, while derivatives in the vertical direction z are represented with second-order centered finite differences. The solution variables are advanced in time using a second-order explicit Adams-Bashforth rule. In order to prevent the buildup of aliasing errors, the upper $1/3$ of wavenumbers are truncated in Fourier space. The flow variables carried throughout the simulation are the three velocity components u, v, and w, the virtual potential temperature θ, and the SGS kinetic energy ϵ. A Poisson equation for the fluctuating pressure P is solved at each time step. The formulation and implementation of that equation ensures that the flow remains incompressible. Two passive, conservative scalars, referred to as B and C scalars, are also tracked during the course of a simulation. The scalar distributions were designed to mimic transport of a "top-down" scalar C with zero surface flux while the scalar B, which is designed to mimic humidity, has nonzero fluxes at both the ground and inversion height.

The flow is horizontally homogeneous, and periodic boundary conditions are used in both horizontal directions. Along the upper boundary, the radiative boundary conditions of Klemp and Durran (1983) for the vertical velocity and pressure are used, the SGS energy is set equal to zero, the virtual potential temperature gradient is taken to be a constant, and the vertical gradient of the horizontal velocity is set equal to zero. At the lower boundary, horizontally averaged conditions at the first computational grid point above the surface are matched to Monin-Obukhov similarity theory (Businger et al., 1973). This yields a prediction of the horizontally averaged surface shear stress and the heat flux. In order to estimate the local, fluctuating surface fluxes, a "local similarity rule" is adopted; it relates the fluctuating value of the surface fluxes to the fluctuating velocity and temperature at the first grid level (See Moeng, 1984 and Sullivan *et al.*, 1994). In the LES the surface boundary condition for scalars is handled in a similar way.

The subgrid-scale (SGS) parameterization used in the LES code is based on a prognostic equation for the SGS turbulent kinetic energy. The kinetic energy is then used to calculate the SGS fluxes.

3.2. LES DATABASE

For the present evaluation, the database generated by LES is mainly confined to cloud-free PBLs driven by shear and buoyancy. Unstable and neutrally stratified PBLs were generated by specifying the surface heat flux, while the shear forcing was introduced by varying the level and vertical distribution of the geostrophic wind. This flow regime was selected because PBLs are typically subjected to this type of forcing, and because of the practical limitations associated with LES. We wish to consider flow regimes where the LES data are relatively independent of the SGS model, so the LES data can be considered as representative of real PBL flows. For this reason, we have omitted the stable regime from the evaluation. The neutral and convective regimes considered are in no way exhaustive in terms of the possible PBL flows, but they do represent a significant subset from which PBL models can be evaluated.

3.2.1. *Case Descriptions*

A summary of the LES database is provided in Tables III and IV. Parameters included in Table III, in addition to the case name, are the following: L_x, L_y, L_z, domain sizes in x, y, z directions; Q_*, surface heat flux; U_g, V_g, geostrophic wind components in x, y directions; $z_{0(u,t,b,c)}$, roughness lengths for momentum, heat and scalars. Here we note that the value of z_0 used for the EKM case is different than the remaining cases and that the roughness length used is the same for momentum, heat and scalars. Table IV gives L and z_i/L where L is the Obukhov length; z_i, the height of the capping inversion; w_*, convective velocity scale; u_*, friction velocity; τ, large-eddy turnover time. We also list in Table IV the method for computing z_i, which is described later.

The convective velocity scale in Table IV is

$$w_* = (\beta Q_* z_i)^{1/3}, \tag{1}$$

where $\beta = g/\theta_0$ is the coefficient of thermal expansion. A large-eddy turnover time is defined as

$$\tau = z_i/w_* \tag{2}$$

for convective cases and

$$\tau = z_i/u_* \tag{3}$$

for shear cases where $w_* = 0.0$. These simulations can be roughly grouped into four different categories.

Free-convection simulation

Case 24F is a simulation of a free-convection PBL; i.e., one with zero mean wind. A strong capping inversion is imposed at 1000 m in order to limit the growth

Table III
Case/Parameter matrix .

Case	L_x, L_y, L_z (km)	Q_*(K m s^{-1})	U_g (m s^{-1})	V_g (m s^{-1})	$z_{0(u,t,b,c)}$ (m)
EKM	$2 \times 2 \times 3.6$	0.00	10.0	0.0	0.10
00WC	$5 \times 5 \times 2$	0.00	15.0	0.0	0.16
05WC	$3 \times 3 \times 1$	0.05	15.0	0.0	0.16
00SC	$3 \times 3 \times 1$	0.00	15.0	0.0	0.16
03SC	$3 \times 3 \times 1$	0.03	15.0	0.0	0.16
05SC	$3 \times 3 \times 1$	0.05	15.0	0.0	0.16
24SC	$5 \times 5 \times 2$	0.24	15.0	0.0	0.16
24F	$5 \times 5 \times 2$	0.24	0.0	0.0	0.16
15B	$5 \times 5 \times 2$	0.15	10.0	0-20	0.16
24B	$5 \times 5 \times 2$	0.24	10.0	0-20	0.16

Table IV
Case/Parameter matrix .

Case	$-z_i/L$	L (m)	z_i (m)	w_* (m s^{-1})	u_* (m s^{-1})	τ (s)	z_i Method
EKM	0.0	∞	1500	0.00	0.390	3600	II
00WC	0.0	∞	1065	0.00	0.667	1596	III
05WC	2.26	-480.7	1087	1.20	0.680	905	III
00SC	0.0	∞	448	0.00	0.500	896	III
03SC	1.30	-379.4	493	0.79	0.530	624	I
05SC	1.30	-369.7	480	0.93	0.623	516	I
24SC	18.4	-55.9	1025	2.00	0.566	512	I
24F	∞	0.00	1033	2.00	0.00	515	I
15B	7.73	-125.3	968	1.68	0.627	576	I
24B	12.1	-83.47	1011	1.99	0.640	508	I

of the PBL with time. The large computational domain is chosen to capture the well-known large thermal plumes which exist for this type of flow (Schmidt and Schumann, 1989).

Buoyancy with shear simulations

This series includes cases 00WC, 05WC, 00SC, 03SC, 05SC, 24SC. All of these runs include various combinations of shear and buoyancy forcing varying from strongly buoyant flows with small shear, case 24SC, to cases with zero buoyancy and strong shear, case 00SC. These flows contain both thermally driven plumes and organized streaky structures (Moeng and Sullivan, 1994). Two types of capping inversions were used in these PBL simulations; it is strong in cases ending with SC and weak in cases ending with WC.

Baroclinic simulations

Two simulations with varying amounts of baroclinic forcing, 15B and 24B, were also considered. As in the previous simulations, these contain strong capping inversions and varying amounts of surface buoyancy forcing. Here, however, baroclinic effects were introduced by varying the geostrophic wind with height.

Ekman simulation

A simulation of an idealized Ekman flow, case EKM, was also included in the present database. This flow is further described in Andrén and Moeng (1993).

3.2.2. *Construction of Simulations*

All simulations were carried out using meshes of 96 points along each coordinate direction (i.e., a total of 96^3 points), except for the Ekman simulation which uses a mesh of $80 \times 80 \times 120$. A uniform equidistant mesh spacing was used in x and y while a uniform spacing, typically smaller than in the horizontal, was used in the vertical direction z.

The simulations were initiated with small perturbations except for the cases with zero surface heat flux. In these cases, sustained turbulence was established by first running several large-eddy turnover times with a small surface heat flux and setting this flux to zero after the turbulence was reasonably established. In this instance, a shear-driven turbulent state was easy to achieve and maintain (Moeng and Sullivan, 1994). A special initiation procedure was used for the Ekman simulation as described in Andrén and Moeng (1993).

The heat flux at the lower boundary was specified for all simulations. A zero surface flux boundary condition was used for the scalar C' in all simulations. The surface boundary condition for the B scalar differs in that a constant value was used, ($B = 15$ arbitrary units). The initial profiles for the passive scalars were constructed from the following rules:

$$\begin{aligned} B &= 13.5, \quad 0 < z \leq 1.01 z_i \\ &= 3.0, \quad z > 1.01 z_i \end{aligned} \tag{4}$$

$$\begin{aligned} C &= 0.0, \quad 0 < z \leq 1.01 z_i \\ &= 1.0, \quad z > 1.01 z_i. \end{aligned} \tag{5}$$

The duration of the simulations was determined by examining the variation in the computed statistics. After some testing, it was decided that the dynamical fields were reasonably well behaved after about 5τ, i.e., after about 5 large-eddy times. At this point the B and C' scalars were injected into the flow using the initial and boundary conditions given above and all fields were then advanced at least another 10τ. The long LES integration periods allow the initial transients to die out and yield a good approximation to statistically stationary data. A sketch of the LES time integration sequence is given in Figure 1.

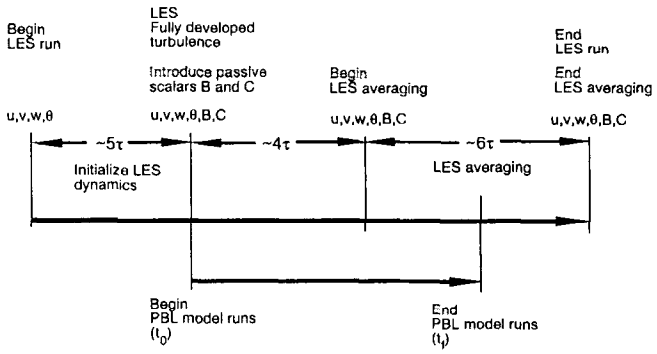

Figure 1. Typical integration sequence.

3.3. Post-Processing of LES Data

The LES generates time and spatially varying dynamical fields u, v, w, θ, e, and P and passive scalar fields B and C, from which one can calculate statistics. We have restricted our attention to means and second-order statistical quantities, as these are of primary importance in a large-scale model. Since LES generates large amounts of information it is not practical to store data at every time step. Instead, we archived selected data at particular time steps and then subsequently analyzed them, choosing enough time steps to obtain reliable statistics.

In calculating statistics we used a combination of temporal and horizontal spatial averages, the latter permitted because of the horizontal homogeneity. A horizontal average of any flow variable $F(x, y, z, t)$, written in discrete variables, is

$$\langle F \rangle(z) = \frac{1}{N_y N_x} \sum_{k=1}^{N_y} \sum_{j=1}^{N_x} F(x_j, y_k, z, t) \,, \tag{6}$$

where the function evaluated at the nodes x_j, y_k is $F(x_j, y_k, z, t)$ and N_x and N_y are the number of grid points in the x and y directions, respectively. For a statistically steady flow, $\langle F \rangle$ is only weakly dependent on time t.

We found that reliable estimates of higher order statistical moments typically cannot be obtained from a spatial average at one time due to the limited number of LES grid points. Smooth estimates can, however, be obtained by further averaging the data in time. One could calculate this spatial average at several different times and average the results. This would ignore the growth of the PBL depth in time, which can be appreciable for convective cases with weak capping inversions. In order to account for this growth, we estimate the PBL height z_i at the sampling time, compute a normalized coordinate z/z_i, nondimensionalize the horizontally averaged statistics by appropriate velocity and temperature scales, interpolate the results to a common grid of z/z_i values, and time-average these gridded values. We then form the dimensional result by multiplying by the average values of the

velocity and temperature scales. In general, between 20 and 30 time samples were used for the averages presented here. Therefore, approximately $2 - 3 \times 10^5$ data points were averaged at every vertical location. All flux estimates include resolved and SGS contributions; i.e., the total average flux computed from the LES data is used for the model comparison.

Since our averaging procedure relies on the boundary-layer height, an estimate of z_i is needed for each type of PBL flow. We considered three different rules for estimating z_i in the LES cases.

Method I (convective method): the height of the minimum total heat flux,

$$\min(\overline{w\theta}(z)) \,. \tag{7}$$

Method II (shear method): the height where the total momentum flux first falls below a specified fraction of the surface stress,

$$\|\overline{uw}(z) + \overline{vw}(z)\| = 0.05 u_*^2 \,. \tag{8}$$

Method III (weak-capping-inversion method): the height where the local average virtual potential temperature $\langle\theta(z)\rangle$ first exceeds the vertical running average of the mixed layer virtual potential temperature by a specified amount, in this case 0.25 K,

$$\langle\theta(z)\rangle \geq \frac{1}{z}\int_0^z \langle\theta(z)\rangle \, dz + 0.25. \tag{9}$$

Different methods of inferring z_i were used because of the wide range of buoyancy and shear forcing and the varying capping inversions. For example, our simulation of the turbulent Ekman flow does not have a capping inversion and thus method II was used to estimate the boundary-layer height. When all three z_i methods apply, as in the convective cases with weak capping inversions, we found that methods I and II yield slightly lower estimates of the boundary-layer height than method III. Method III is the most robust, being relatively invariant to wide variations in the entrainment heat flux which can occur for weakly capped cases with small or zero surface heat flux. The z_i method used for each simulation is given in Table IV. For the PBL models, method III was used for all cases except the Ekman flow, which used method II.

4. The PBL Models

4.1. General Model Description

There are several different methods by which turbulence effects in a large-scale model are treated. One method represents the turbulent flux term in each mean-field

equation through an eddy diffusivity. In a horizontally homogeneous PBL and in the absence of radiative flux divergence these mean-field equations then become

$$\frac{dU}{dt} = f(V - V_g) + \frac{\partial}{\partial z}\left\{K_m \frac{\partial U}{\partial z}\right\}, \tag{10}$$

$$\frac{dV}{dt} = f(U_g - U) + \frac{\partial}{\partial z}\left\{K_m \frac{\partial V}{\partial z}\right\}, \tag{11}$$

$$\frac{d\phi}{dt} = \frac{\partial}{\partial z}\left\{K_\phi \frac{\partial \phi}{\partial z}\right\} \tag{12}$$

in which ϕ is θ, B or C. The $K(Ri)$ and low order single-point closures differ mainly in their specification of the eddy diffusivities (K_m and K_ϕ). The K-profile model uses nearly identical equations but has a "non-local" term in the flux-gradient relation for temperature.

There are also closures that are not based on the explicit solution of differential equations. The multi-stream exchange and stability-bounds schemes are in this category. These closures, although based on physical principles, take the form of one or more "mixing rules" to carry out mixing of properties between different regions of the fluid. Both the mixed-layer model and the stability-bounds model make assumptions about the structure of the mixed layer and the distribution of fluxes within it.

At this point it is worth explaining our interpretation of the term "non-local". The term non-local is one which is somewhat muddied by its use in a number of contexts. Here we intend it to mean that mixing at a point in the profile is *physically* related to properties or processes at some point which is not adjacent to that point. This really has two interpretations. The first is in the real atmosphere where, for example, large plumes which scale with the depth of the mixed layer impinge on the capping inversion. In this region, the mixing which occurs is dependent upon not only the local properties of the flow but those which are transported from some distant point, in this case near the surface. The buoyancy and the mechanical energy with which the plume interacts with the inversion is determined from flow properties much nearer the surface than the capping inversion. Here we note that this non-local behaviour is reasonably well represented in LES by virtue of the fact that these plumes are resolved.

In the case of the closure models, there are a number of degrees of non-local behaviour formulated into the models. The transilient model, for example, is explicitly non-local in that it mixes parcels from widely separated points in the profile. One might think of this type of model as having *first-order* non-local characteristics. Alternately, models such as the K-profile model mix properties from points which are adjacent, however, this is done with mixing coefficients which are determined using properties of the flow in areas which are not adjacent to the point. One might think of this as a *second-order* non-local property.

4.2. Boundary Conditions

One challenge of this comparison exercise is to provide a framework within which all of the models can be compared fairly. To ensure that differences in the profiles produced by different models are intrinsic to the models rather than details of their implementation, wherever possible the models share common service routines for the calculation of boundary conditions, initialization, and time integration.

In all but the mixed-layer model, boundary conditions are handled by common routines that use Monin-Obukhov similarity theory and the Businger-Dyer relationships,

$$\frac{U}{u_*} = \frac{1}{\kappa}\left[\ln\left(\frac{z+z_0}{z_0}\right) - \Psi_m\left(\frac{z}{L}\right)\right] \tag{13}$$

$$\frac{\phi - \phi_0}{\phi_*} = \frac{1}{\kappa}\left[\ln\left(\frac{z+z_0}{z_0}\right) - \Psi_h\left(\frac{z}{L}\right)\right] \tag{14}$$

$$L = -\frac{u_*^3\theta_0}{\kappa g\langle w'\theta'\rangle_0} \tag{15}$$

where ϕ is one of θ, B or C, ϕ_0 is $\phi(z_0)$ and

$$\Psi_m = \Psi_h = -5\frac{z}{L}, \qquad \frac{z}{L} \geq 0 \tag{16}$$

$$\Psi_m = \ln\left[\left(\frac{1+x^2}{2}\right)\left(\frac{1+x}{2}\right)^2\right] - \tan^{-1}x + \frac{\pi}{2}, \qquad \frac{z}{L} < 0 \tag{17}$$

$$\Psi_h = 2\ln\left(\frac{1+x^2}{2}\right) \qquad \frac{z}{L} < 0 \tag{18}$$

where

$$x = (1 - 15z/L)^{1/4} \tag{19}$$

(from Arya, 1988).

We use a no-slip lower boundary condition for velocity and a constant-flux boundary condition for θ. We specify a constant value of the B scalar at the surface, allowing the surface flux to vary according to Equation (14). A zero-flux lower boundary condition is specified for the C scalar.

The mixed-layer model is handled somewhat differently from the rest in the calculation of surface fluxes. As implemented by Suarez *et al.* (1983) in the UCLA general circulation model, we use the bulk aerodynamic formulation described by Deardorff (1972b). This method uses a combination of surface-layer and PBL-deficit formulations to specify the friction and heat-transfer coefficients,

$$C_u \equiv \frac{u_*}{U_m} \tag{20}$$

and

$$C_\theta \equiv \frac{-\langle w'\theta' \rangle_0}{u_*(\theta_m - \theta_0)} \tag{21}$$

where the subscript m signifies the mean mixed layer value and C_u and C_θ are functions of z_i/z_0 and z_i/L. Scalars are handled similarly using C_θ,

$$-\langle w'b' \rangle_0 = u_*(B_m - B_0)C_\theta \tag{22}$$

$$-\langle w'c' \rangle_0 = u_*(C_m - C_0)C_\theta. \tag{23}$$

This allows the determination of surface fluxes from mean mixed-layer values.

Because not all of the models explicitly calculate turbulent fluxes, the fluxes are derived diagnostically from the mean conservation equations. This is accomplished by vertical integration of the time tendency of the mean fields,

$$\frac{\partial \phi(z,t)}{\partial t} = \frac{\partial \langle w'\phi' \rangle(z,t)}{\partial z} + S(z,t) \tag{24}$$

where ϕ is U, V, θ, B or C and S is a source term (for example $f(V - V_g)$ when $\phi = U$). Integration of this source term with the surface flux as a lower boundary condition yields the flux profile,

$$\langle w'\phi' \rangle(z,t) = \int_0^z \frac{\partial \phi(z',t)}{\partial t} \mathrm{d}z' + \int_0^z S(z',t)\mathrm{d}z' + \langle w'\phi' \rangle(z_0,t). \tag{25}$$

5. Modelling Experiments

5.1. Integration Sequence

As shown in Figure 1, the experiments begin by running the LES code for a time sufficient to produce fully developed, quasi-steady turbulence fields. Scalars are then introduced into the LES flow; the LES code then continues to run and the integration of the PBL models begins. Initial conditions for the PBL models are taken from horizontal averages of the U, V and θ fields from the LES and the prescribed profiles for the B- and C-scalars. In most cases the grid spacing of the PBL models is greater than that of the LES, requiring the LES profiles to be averaged over the intervals of the PBL model grid (or over the entire mixed layer, in the case of the mixed-layer and stability-bounds models.) From this point, both the LES and PBL models are integrated for about ten large-eddy-turnover times. During this integration, both the LES and PBL models have the same surface heating and Coriolis forcing.

Figure 2 shows the LES and PBL model final mean profiles for the 24SC case as used in the comparison. Strong shear in both U and V is present at the top

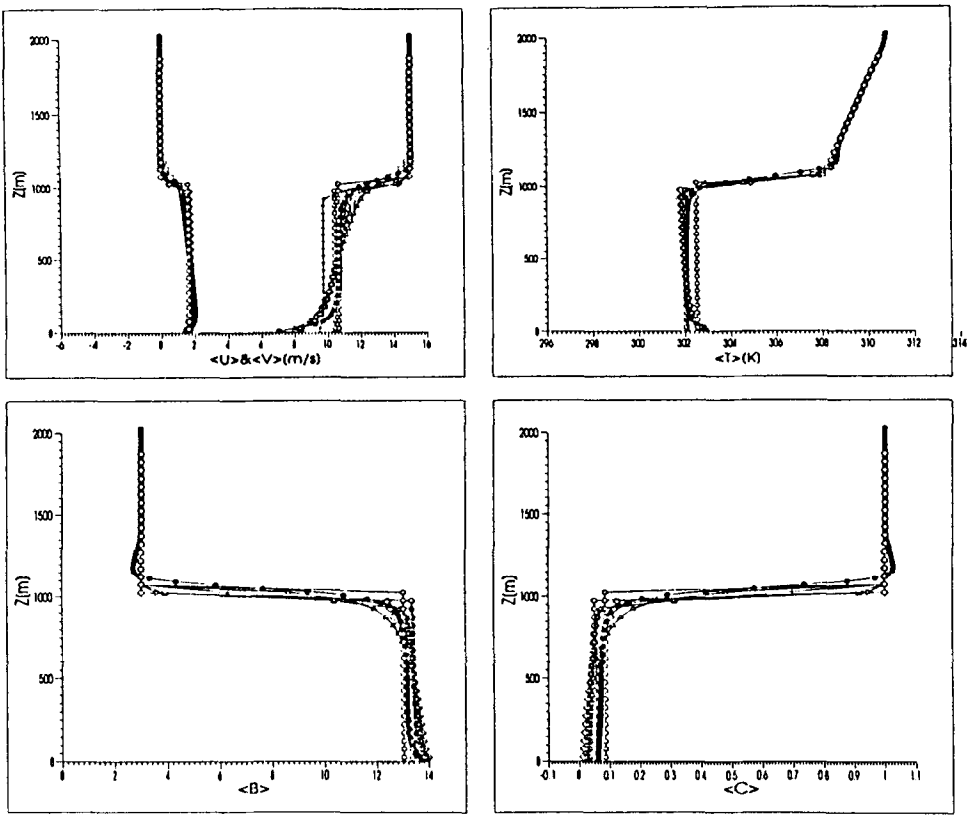

Figure 2. Mean final profiles for the 24SC case. PBL model resoultion is 50 m.

of the mixed layer. The potential temperature profile shows the strong capping inversion while both scalars have a sharp jump located at the inversion base. The main difference between this and the weakly capped cases is the strength of the capping inversion, here on the order of 6 K while the weakly capped case is near 1 K.

The mixed-layer model, here shown as open hexagons projected onto a 50 m grid, is initialized differently from the grid-point models. The algorithm for initializing mean fields in the mixed-layer model linearly extrapolates the profile above the mixed layer down to the top of the mixed layer. The jump at the top of the mixed layer is then calculated as the difference between the mean value within the mixed layer and the value at the base of the inversion. Within the model this is maintained as a step change at the top of the mixed layer, although the plotted profiles show a change over one grid interval on a 50 m resolution grid. This is purely an artifact of the plotting.

6. Results

Neglecting mean advection and local effects such as radiative flux divergence, the instantaneous change in a variable ϕ is given by

$$\frac{\partial \phi(z,t)}{\partial t} = -\frac{\partial}{\partial z}\langle w'\phi'\rangle(z,t). \tag{26}$$

It follows that any change in potential temperature or scalar concentration averaged over the mixed layer is a result of a change in flux across the mixed layer:

$$\begin{aligned}\frac{\partial \overline{\phi}}{\partial t} &\approx -\frac{1}{z_i(t)}\int_{z_0}^{z_i(t)} \frac{\partial}{\partial z}\langle w'\phi'\rangle(z,t)dz \\ &= -\frac{\langle w'\phi'\rangle(z_i(t),t) - \langle w'\phi'\rangle(0,t)}{z_i(t)}.\end{aligned} \tag{27}$$

This shows that the time rate of change of a mixed layer mean value is proportional to the difference between surface and entrainment fluxes and inversely proportional to the depth of the mixed layer. If we are concerned with mixed-layer-mean values, as seems reasonable in the context of large-scale modelling, we must examine the ability of the models to predict surface and entrainment fluxes.

In order to assess the ability of the PBL models to reproduce mixed-layer profiles of mean variables as well as surface and entrainment fluxes, we have defined two measures of model performance, A_1 and A_2:

$$A_1 \equiv \frac{-\int_{z_i(t_0)}^{H}(\phi(z,t_f) - \phi(z,t_0))dz}{t_f - t_0} = -\int_{t_0}^{t_f} \frac{\langle w'\phi'\rangle(z_i(t_0),t)}{t_f - t_0}dt \tag{28}$$

$$\begin{aligned}A_2 &\equiv \frac{\int_{z_0}^{z_i(t_0)}(\phi(z,t_f) - \phi(z,t_0))dz}{t_f - t_0} \\ &= -\int_{t_0}^{t_f} \frac{\langle w'\phi'\rangle(z_i(t_0),t) - \langle w'\phi'\rangle(z_0,t)}{t_f - t_0}dt.\end{aligned} \tag{29}$$

H is the top of the model and t_0 and t_f are initial and final integration times, respectively.

These measures have a number of advantages over more traditional ones. First, they are easily calculated from final and initial profiles of mean variables and are integral measures of model performance. This is in contrast to measures such as time-integrated entrainment flux at z_i, since for some models z_i and the flux there can fail to be smooth functions of time or even well-defined.

Although it is not a direct measure of entrainment flux, the RHS of Equation (28) represents the average flux through $z = z_i(t_0)$, between t_0 and t_f. Figure 3 shows a schematic of the two model performance measures showing initial and

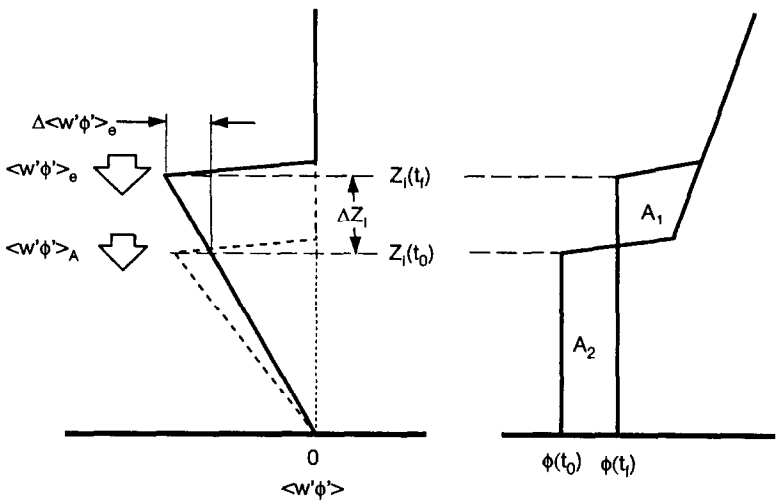

Figure 3. Idealized entrainment diagram. A_1 is entrainment while A_2 includes entrainment and integrated surface flux. A_1 and A_2. On the left is the flux profile at t_f with open arrows showing entrainment flux $\langle w'\phi' \rangle_e$ and the contribution to the A_1 and A_2 entrainment measures $\langle w'\phi' \rangle_A$

final profiles of the variable ϕ with an increase in mixed-layer depth from $z_i(t_0)$ to $z_i(t_f)$. The utility of the A_1 and A_2 measures can be more easily seen by noting the following: $A_2 - A_1$ follows the average surface flux over the period; $A_2 - A_1$ is zero for the C-scalar, with A_1 and A_2 purely functions of entrainment; $A_2 > A_1$ for θ, while for the B-scalar A_2 can be less than A_1 and even negative for large enough entrainment.

As a cautionary note, it should be pointed out that these measures are finite in formulation and are subject to errors which grow as $(\Delta z_i / z_i(t_0))^2$. These measures should not be used where the initial and final values of z_i differ by a significant fraction of the boundary-layer depth. Care has been taken in what is presented here to ensure that this is not the case.

In our description of model results we abbreviate the model types as follows: $K(Ri)$ is KOFR; K-profile, KPRO; Mellor-Yamada level 2, MY20; Mellor-Yamada level 2.5, MY25; transilient, TRAN; stability-bounds, STAB; and mixed layer, MIX. Where case-specific results are presented, the PBL model resolution is 50 metres. As we will show, at this resolution the models show a weak dependence on resolution. This allows discussion of the physical characteristics of the models while resolution is not an issue. The method of generating the PBL model grid for the resolution experiments is described in the discussion of those experiments.

6.1. C-SCALAR

The A_1 measure has been plotted for all of the cases* for the C-scalar in Figure 4. The A_1 values have been normalized by the mean of the A_1 measure for the LES. This normalization was chosen to retain relative magnitudes. Figure 5 shows the mixed-layer mean (between the surface and z_i) concentrations of the C-scalar normalized by integration time and the mean concentration of the C-scalar over all of the LES cases. This normalization allows comparison with the A_1 measure shown in Figure 4. In Figures 4 and 5 the cases are arranged in groups separated by vertical lines. On the left of the figure is the EKM case. Moving to the right, the next two cases are weakly capped cases with limited surface heating (00WC and 05WC). The next four cases (00SC to 24SC) are all identical except that the surface heat flux ranges from 0.0 to 0.24 K m s^{-1} and z_i is of order 1000 m for 24SC and 500 m for the other three cases. These cases are strongly capped (see Figure 2). The next case to the right is a free-convection case (24F) with surface heating equal to that of 24SC but with zero geostrophic wind. The two cases to the extreme right are baroclinic (15B and 24B) in which the geostrophic wind varies with height. They have moderate surface heating, 0.15 K m s^{-1} and 0.24 K m s^{-1}, respectively, and are strongly capped. More details of these runs are found in Tables III and IV.

We expect the mean concentration within the mixed layer to depend on the mean flux divergence throughout the mixed layer and thus scale with total entrainment for similar mixed-layer depths. Thus, the striking similarity between Figures 4 and 5 is not unexpected. These figures show the substantial variation in entrainment and the mean concentration over the cases.

The LES results in Figures 4 and 5 show the strong dependence of entrainment on surface heating. This is particularly strong for the weakly capped cases (00WC and 05WC) but also evident in the strongly capped cases. The effect of mean shear can also be seen in the LES results. The free-convection case (24SC) shows a substantial decrease in entrainment when compared to either of the sheared cases with similar surface heating (24SC and 24B). The two cases with strong geostrophic wind shear (15B and 24B) show the opposite tendency, entraining significantly more than cases with similar surface heating and strong capping inversions (05SC and 24SC).

In most instances the PBL models share responses to surface heating and shear. With the exception of MIX, there is a tendency to underpredict entrainment and therefore mixed-layer-mean concentrations by all of the models. For the weakly capped cases (00WC and 05WC) KPRO and MIX overpredict entrainment while the remaining models underpredict. All of the models underestimate entrainment and mixed-layer concentration for the strongly sheared baroclinic cases (15B and 24B). Here MIX, TRAN and KPRO give results closest to the LES values, while still being somewhat low.

* Scalars are not included in the EKM case and therefore are not plotted or included in averaging over cases.

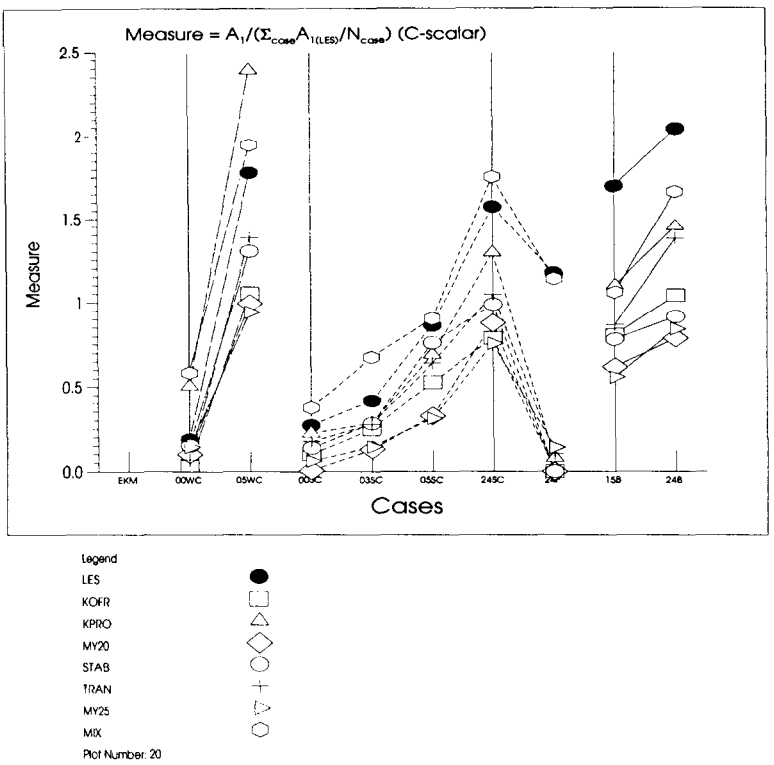

Figure 4. C-scalar A_1 measures normalized by LES A_1 value averaged over cases.

Theory, existing measurements, and LES results all suggest that in a strongly capped environment, the complex interaction between ascending plumes and the capping inversion determines the the rate at which overlying air is entrained into the mixed layer. This interaction is affected by the local shear over the entrainment zone, shear across the entire mixed layer and surface heating. This implies that non-local aspects of mixed-layer structure play a part in determining the entrainment rate.

Therefore it is perhaps not unexpected that the non-local models MIX, TRAN and KPRO give the best results in the strongly capped cases. Each of these embodies some aspect of non-local mixing, with MIX based explicitly on a non-local formulation of entrainment dynamics. MIX predicts results nearly identical to LES for the free-convection case (24F), while the remaining models appear to do very poorly in the absence of shear.

6.2. TEMPERATURE

In the case of potential temperature, we again expect to see entrainment play a role. For cases with large surface fluxes, the role of entrainment is less important

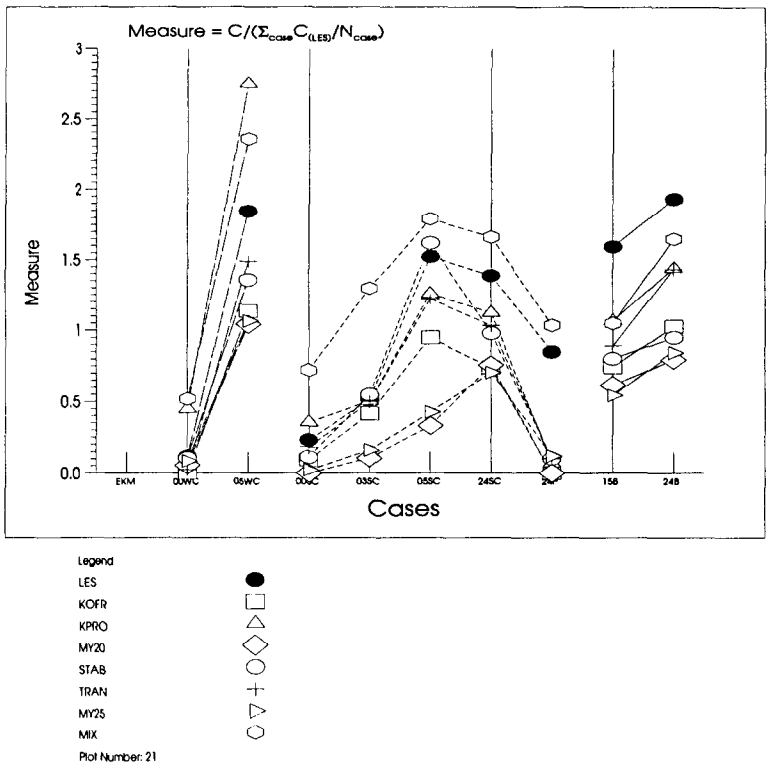

Figure 5. Mixed-layer mean values of C-scalar concentration normalized by LES C-scalar concentration averaged over cases.

because the surface heat flux is responsible for a large portion of the change in mixed-layer-mean potential temperature between initial and final profiles. In terms of our measures, we expect to see A_2 somewhat larger than A_1 for cases with positive surface heat flux.

Figure 6 shows the A_1 measure for potential temperature normalized as before by the average of the LES values of A_1 over the cases. The general response of the LES to shear and surface heating is similar to that of the C-scalar results, with a few exceptions. Of all of the models, only MIX and KPRO show the expected enhanced entrainment with the increase in surface heating between the 05SC and the 24SC cases. Both MY20 and MY25 maintain a nearly constant but substantially underestimated value of A_1, while KOFR and STAB show substantial decreases. Examination of the two cases shows that although the entrainment zone is deeper and the temperature difference across the entrainment zone is less for the 24SC case due to its strong surface heating, the shear across the entrainment zone is substantially less. The local Richardson number across the entrainment zone are 0.44 and 1.60 for the 05SC and 24SC cases respectively. STAB and KOFR are explicitly dependent upon Richardson number while both MY20 and MY25 are

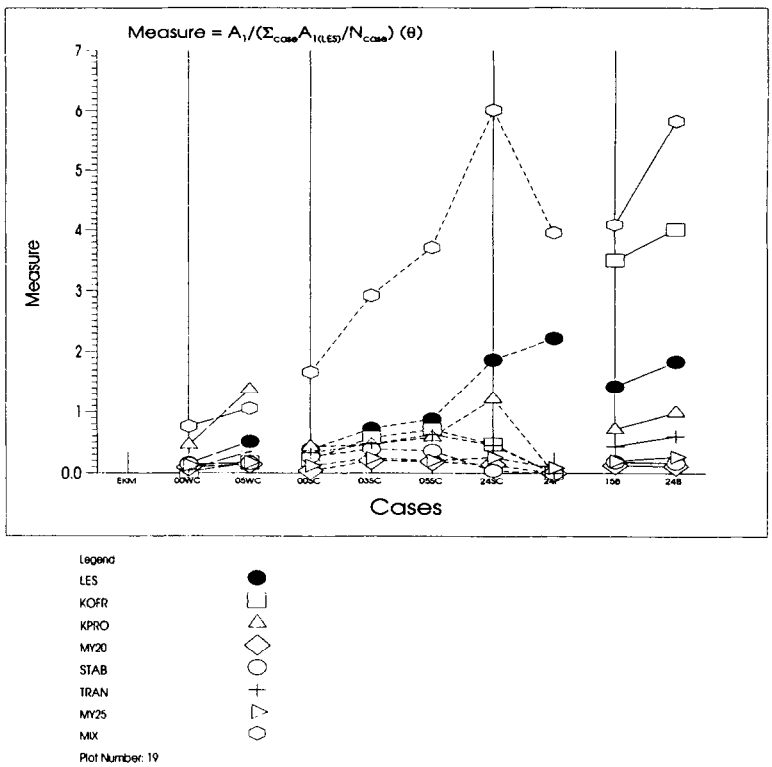

Figure 6. θ A_1 measures normalized by LES A_1 value averaged over the cases.

indirectly dependent upon the local Richardson number. Thus, the diminished shear in the entrainment zone strongly affects their ability to entrain overlying air. The particularly strong dependence on shear in KOFR can also be seen in its over-prediction of entrainment in the baroclinic cases (15B and 24B).

In contrast, TRAN is less dependent upon local Richardson number by virtue of its non-local formulation. While mixing across the entrainment zone is diminished, mixing from the surface, which is independent of the local Richarson number within and near the entrainment zone, maintains some entrainment. KPRO, which is independent of the entrainment zone Richardson number, shows an increase in entrainment with increase in surface heating and performs the best of all of the schemes in this instance.

In the free-convection case (24F), all of the models performed poorly with all but MIX predicting nearly no entrainment and MIX significantly over-predicting entrainment. The overprediction by MIX is consistent for all of the cases. The reasons lie partly in the temperature structure artificially imposed upon the model by the comparison to LES profiles. We can illustrate this through simple plume behaviour in a convective mixed layer. An initially buoyant parcel rising from

the surface will overshoot its level of neutral buoyancy; this occurs where the potential temperature is near that of the surface air. The subsequent overturning and distortion of parcels entrains overlying air into the mixed layer. MIX represents the entrainment flux by the time rate of change of z_i multiplied by a step change in temperature at the top of the mixed layer. Thus, to model the simple mechanism described above, the correct mixed-layer growth rate needs to be combined with a step change that approximates the difference between the surface temperature and the mean mixed layer temperature. In all of the strongly capped cases the imposed strength of the capping inversion is such that $\Delta\theta$ is much greater, often by a factor of two or more, than the difference between the temperature at the surface and that within the mixed layer. Thus, although the mixed-layer depth is well predicted by the MIX model, the entrainment and therefore the mixed-layer mean is in strong disagreement with that of the LES due to the large value of $\Delta\theta$. These results underscore the simplicity of the assumptions implicit in the mixed-layer formulation.

To see more clearly the effect of entrainment on the layer-averaged potential temperature, we turn to Figure 7 which shows the ratios $(A_1/(A_2 - A_1))$ for each of the models in all cases where the surface heat flux is non-zero. This measure mimics the entrainment/surface flux ratio. The LES ratios vary somewhat between cases, decreasing with stronger surface heat flux. For the strongly heated, strongly capped cases (24SC, 24F, 15B and 24B) and the case with weak surface heating and a weak capping inversion (05WC) the ratio is near 0.2, the value often cited for convective boundary layers. With weak surface heating and a strong capping inversion (03SC and 05SC), the value is significantly greater. Thus, the models make the largest errors in cases where entrainment makes the smallest contribution to the mean mixed layer values.

6.3. B-SCALAR

Both the C-scalar and potential temperature use a specified flux at the lower boundary. The B-scalar is more like moisture, with its surface flux dependent upon the difference between a specified surface value (15.0) and the mixed-layer mean. The initial profile of the B-scalar has a constant value (13.5) in the mixed layer with a step change to a value of 3.0 above the mixed layer. This concentration profile initially induces large surface and entrainment fluxes of B-scalar. As integration proceeds, air with lower B-scalar concentration is entrained, acting to reduce the concentration in the mixed layer. Thus, as with potential temperature, the mixed-layer concentration of the B-scalar depends on both the entrainment and surface fluxes.

Figure 8 shows the A_2 measure for the B-scalar, with typical concentration profiles given in the lower right of the figure. The solid line is the initial B-scalar concentration profile with profiles 1-3 representing different balances between upward surface flux and entrainment flux. Profile 1 shows the results of strong

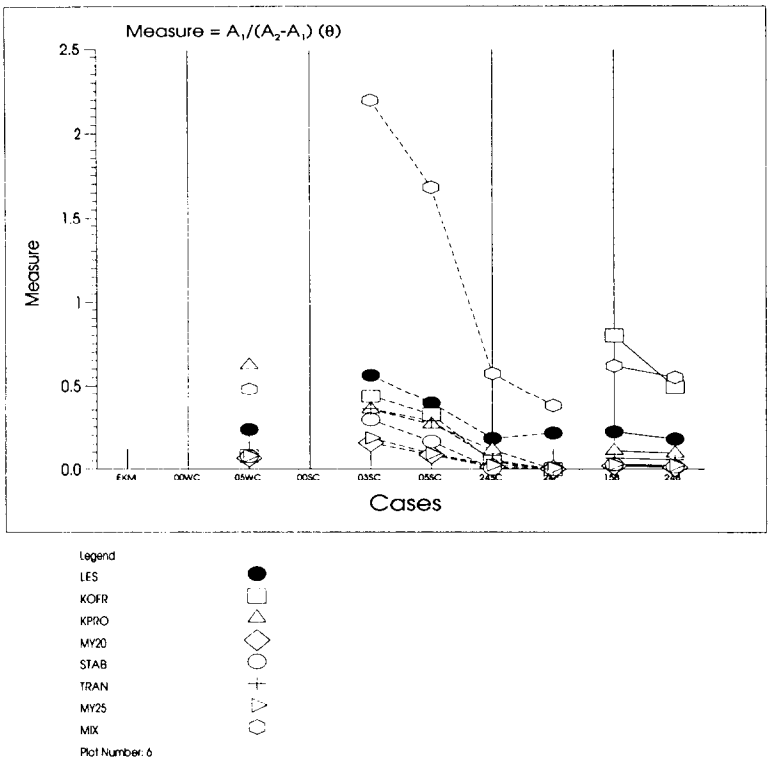

Figure 7. Integrated entrainment ratio $(A_1/(A_2 - A_1))$ for θ.

entrainment with weak surface flux, while profile 3 shows the opposite balance; profile 2 lies between the others. Given the definition of A_2, we expect that an underestimate of entrainment or an overestimate of surface flux yields values of A_2 lower than the LES. The similarities between the plots of A_1 for θ and particularly the C-scalar suggest that entrainment is underpredicted in the strongly capped cases and overpredicted in the weakly capped ones. This is to be expected, since the nearly constant, large step change in concentration at the top of the mixed layer is similar to that of the C-scalar. This suggests that the main contributor to the mixed-layer concentration of the B-scalar is again entrainment.

6.4. Momentum

The momentum budget within the mixed layer and entrainment zone is somewhat more complex than that of either the C-scalar or the potential temperature (θ). The vertical integrals of the horizontal momentum equations are

$$\int_{z_0}^{H} \left[\frac{\partial U}{\partial t} - f(V - V_g) \right] dz = -\langle u'w' \rangle_{z_0} \tag{30}$$

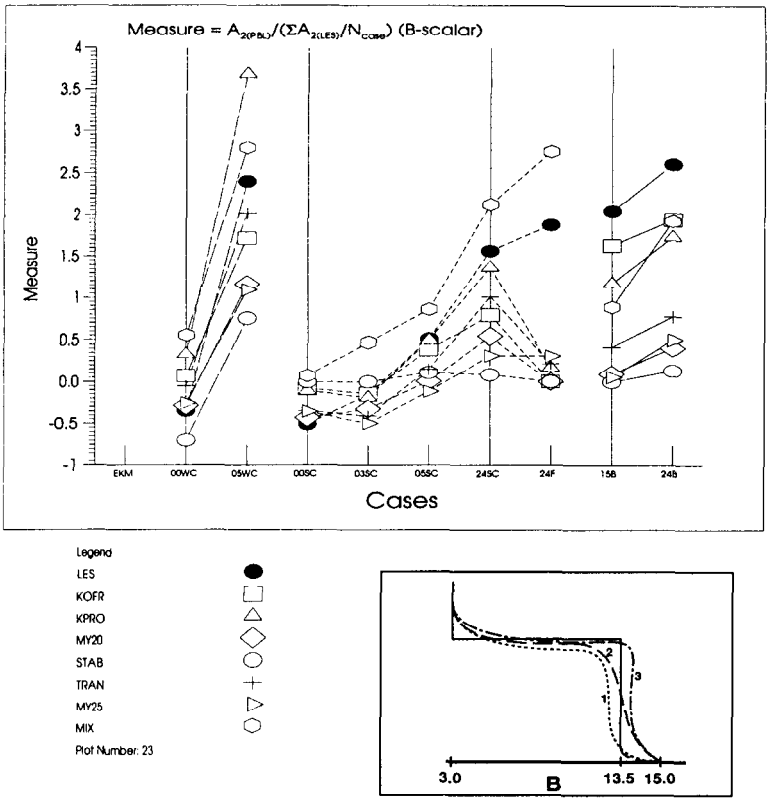

Figure 8. B-scalar A_2 measures normalized by LES A_2 value averaged over cases.

and

$$\int_{z_0}^{H} \left[\frac{\partial V}{\partial t} - f(Ug - U) \right] dz = -\langle v'w' \rangle_{z_0} \tag{31}$$

where H is the top of the model and the subscript z_0 indicates a value at height z_0. Because of the geostrophic-departure terms in the integrals, the simple conservation arguments we used earlier for scalars do not apply here. Instead, we will focus on the ability of the PBL models to predict surface shear stress. Figure 9 shows a comparison of u_* from PBL and LES models, normalized with the LES results. The error is only weakly systematic; MY20 and MY25 consistently underpredict, TRAN consistently overpredicts, and the remainder show a mix of over- and underprediction. Most of the errors are well within the 15-25 percent range, suggesting reasonable performance in predicting surface momentum flux. The consistent over-prediction in the EKM case may be less a reflection of the performance of the PBL models than the poor treatment of small near-surface eddies by the LES model under neutral stratification.

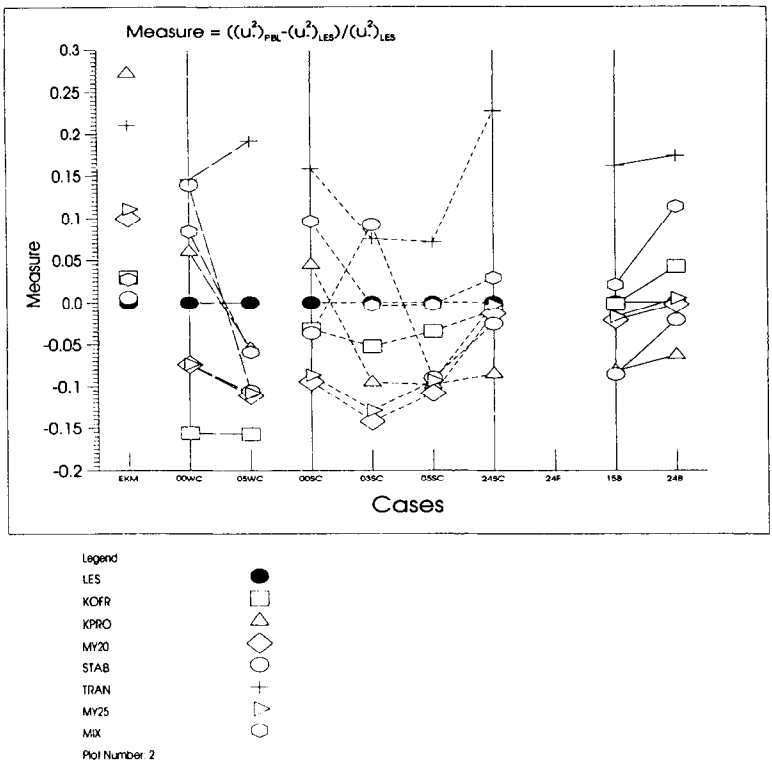

Figure 9. Difference between PBL models and LES for surface momentum flux normalized by $(u_*^2)_{LES}$.

6.5. Resolution-Dependent Measures

A number of practical factors must be considered in the choice of a closure scheme for use in a large-scale model. These include the ease of implementation of the closure into the code structure as well as its computational cost. Including more points within the mixed layer generally leads to a more accurate calculation, due to the enhanced ability of the grid-point schemes to resolve mean gradients. This tradeoff between cost and accuracy leads to the concept of optimal resolution.

We have defined and calculated two additional measures of model performance with the notion of optimal resolution in mind. The first, shown in Figure 10, measures a model's ability to calculate mean values. The variables included in the measure are θ, the B-scalar, the C-scalar, and $|V|$ (wind speed, $(U^2+V^2)^{1/2}$). The second, shown in Figure 11, measures a model's ability to calculate surface and entrainment fluxes. The fluxes in this measure are $\langle w'\theta'\rangle_e$, $\langle w'b'\rangle_{sfc}$, $\langle w'c'\rangle_e$ and u_* $((\langle w'u'\rangle_{sfc}^2+\langle w'v'\rangle_{sfc}^2)^{1/4})$. These two measures are averaged over the modelled cases and therefore indicate the expected error over the range of atmospheric stabilities and thermal structures in the comparison.

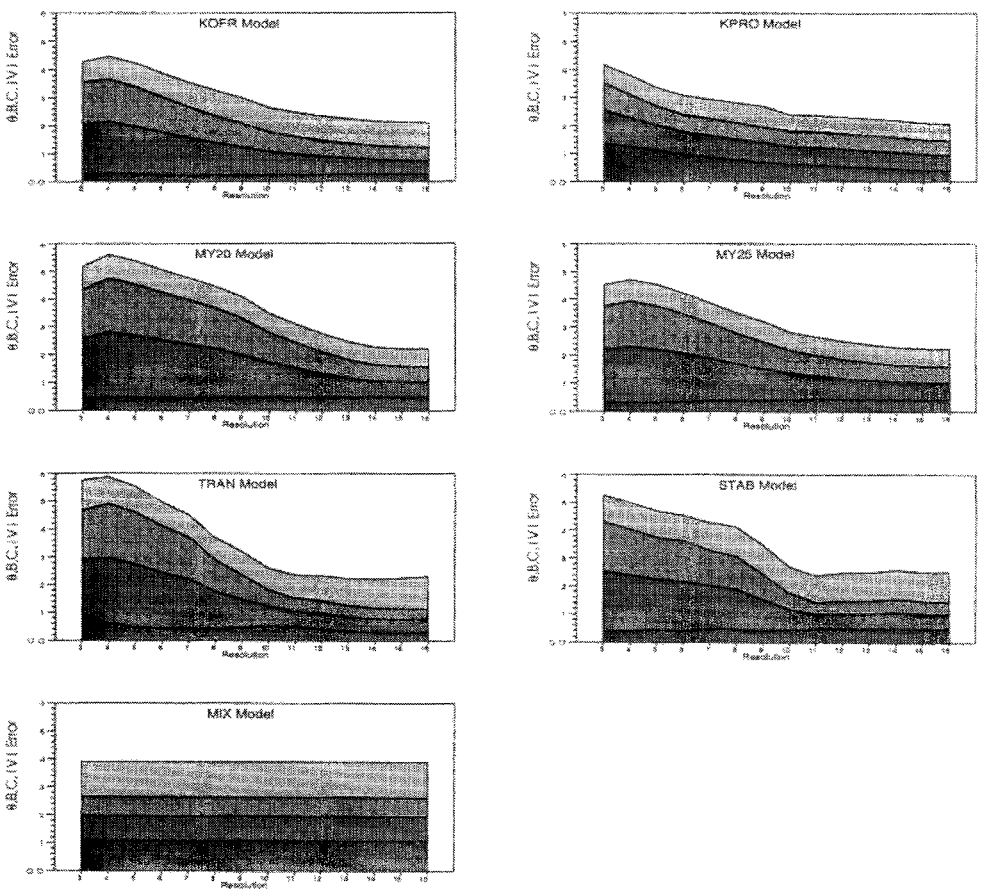

Figure 10. Aggregate error averaged over all cases for θ, B-scalar, C-scalar and wind speed $|V|$ (bottom to top) plotted against resolution. Numbers along abscissa are number of grid lengths (Δz) in the mixed layer. Error measures and normalization are described in text.

To show the dependence of model performance on resolution, as indicated by the above measures, the models were run at a number of resolutions. The resolution, as plotted on the abscissa in Figures 10 and 11, is defined as the number of grid lengths (Δz) within the mixed layer. Resolutions used in the experiment range from 3 to 15, or between $\approx$ 330 m ($z_i \approx 1000$ m, 3 points) and $\approx$ 33 m ($z_i \approx 500$ m, 15 points) depending upon mixed-layer depth and the number of grid points. The latter represents a somewhat optimistic estimate of the upper limit that can be used within large-scale models.

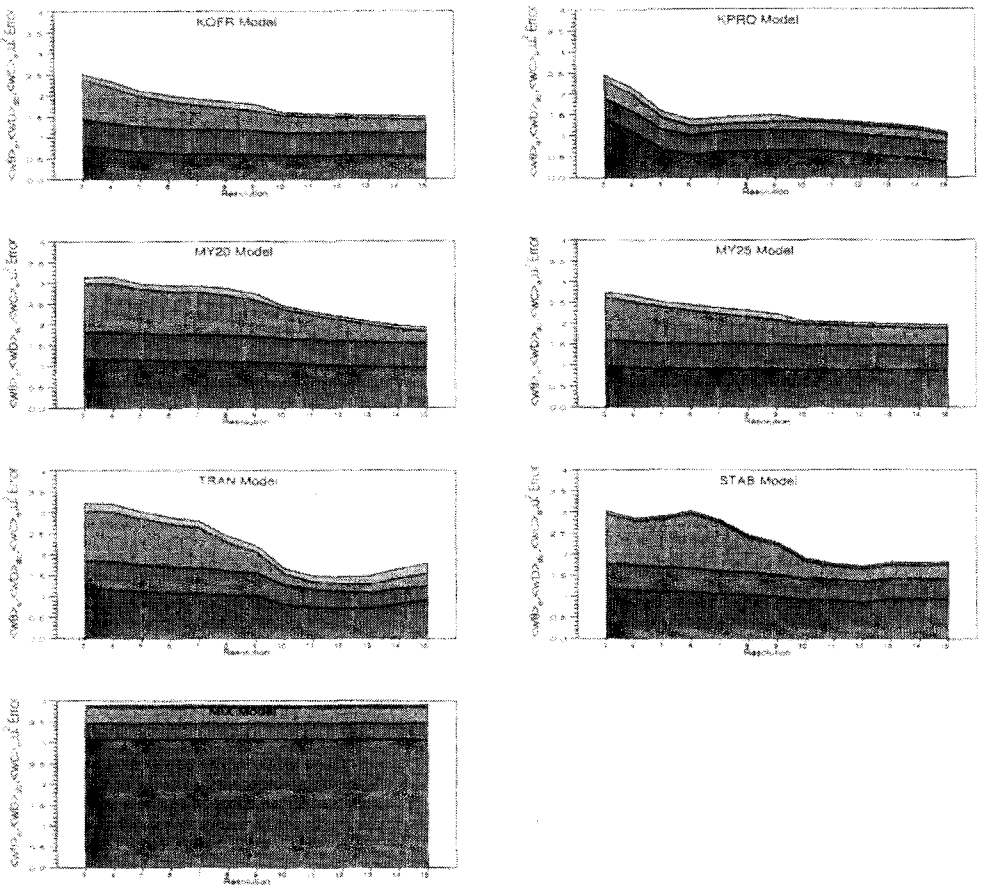

Figure 11. Aggregate surface and entrainment flux error for $\langle w\theta \rangle_s$, $\langle wb \rangle_{sfc}$, $\langle wc \rangle_s$ and u_* (bottom to top) averaged over all cases, plotted against resolution. Numbers along abscissa are number of grid lengths (Δz) the mixed layer. Error measures and normalization are described in text.

6.5.1. *Aggregate Mean Profile Error*

The measure shown in Figure 10 is based on the difference between model and LES values at the final integration time (t_f) at different levels (z_j) throughout the modelled profiles,

$$e_j(\phi) = \frac{\overline{\phi}(z_j, t_f)_{LES} - \phi(z_j, t_f)_{model}}{(t_f - t_i)} \tag{32}$$

where ϕ is any mean variable and t_i and t_f are respectively the initial and final times in the model integration. Here the overbar on ϕ represents the LES value, found by averaging over one PBL-model grid length centered on z_j. These error

measures are incorporated into an rms estimate of the error over the mixed layer for each case,

$$\epsilon(\phi)_{case} = \left[\frac{1}{N_{z_i}+1} \sum_{j=1}^{N_{z_i}+1} e_j(\phi)^2 \right]^{1/2} \tag{33}$$

where N_{z_i} refers to the number of points in the PBL-model mixed layer. The rms profile errors are then normalized by Φ, the change in the mean profile averaged over profiles and cases for the LES,

$$\Phi = \frac{1}{N_{LES} N_{case}} \sum_{j=1}^{N_{LES}} \sum_{case=1}^{N_{case}} \frac{|\phi(z_j, t_f)_{case} - \phi(z_j, t_i)_{case}|}{(t_f - t_i)_{case}}. \tag{34}$$

Here N_{LES} refers to the number of points in the LES profiles and N_{case} is the number of cases over which the average is taken.

An aggregate rms error is then calculated using the normalized measures, providing a performance measure over the parameter space in the study:

$$E(\phi) = \left[\frac{1}{N_{case}} \sum_{case=1}^{N_{case}} \left(\frac{\epsilon(\phi)_{case}}{\Phi} \right)^2 \right]^{1/2}. \tag{35}$$

In Figures 10 and 11, the error values are plotted one above the other to show the cumulative error as well as the individual contributions to the total error from each variable. Figure 10 shows a marked similarity of the response to resolution, particularly near the high-resolution end of the plot. All of the grid-point models show similar performance at high resolution, differing substantially only at coarse resolutions. Both TRAN and STAB become independent of resolution near 10 Δz, while the remaining grid-point models show an error which is significantly reduced but still diminishing with increasing resolution. At very low resolutions (near 3 Δz), both KPRO and KOFR appear to give the lowest aggregate mean profile error between the models. MIX is independent of resolution and gives errors that are similar to most of the grid-point models run at between 6 and 9 Δz and similar to KPRO near 4 Δz.

6.5.2. *Aggregate Flux Error*

In order to examine the error associated with the over- or under-prediction of surface and entrainment fluxes, an aggregate index of flux error was defined and calculated. Like the aggregate mean profile error ($E(\phi)$), the aggregate flux error uses an average over cases.

The aggregate flux error uses the modelled flux (entrainment or surface) integrated between initial and final model integration times, divided by the length of the integration,

$$f(\phi)_{case} = \frac{\int_{t_i}^{t_f} \langle w'\phi' \rangle_{(e/s)} dt}{(t_f - t_i)}. \tag{36}$$

Here the subscripts e and s refer to entrainment or surface values respectively. The entrainment flux is defined as the instantaneous minimum value of $\langle w'\phi' \rangle$, while surface fluxes are extracted at z_0.

The basic element of the error measure is the difference between the model and LES values of the integrated flux for each case normalized by the total flux over all of the cases,

$$e(\phi)_{case} = \frac{(f(\phi)_{case})_{PBL} - (f(\phi)_{case})_{LES}}{\frac{1}{N_{case}} \sum_{case=1}^{N_{case}} (f(\phi)_{case})_{LES}}. \tag{37}$$

This normalization implies a weight for each case which is proportional to the strength of the flux for the case. The per-case error is then used to calculate an rms error over the cases for each resolution,

$$F(\phi) = \left[\frac{1}{N_{case}} \sum_{case=1}^{N_{case}} e(\phi)_{case}^2 \right]^{1/2}. \tag{38}$$

Figure 11 shows the expected dependence on resolution of the surface and entrainment fluxes, again noting the mixed-layer model's independence due to its formulation. Although it is difficult to compare directly the relative errors between the variables, it is clear that the entrainment flux of the C-scalar is the most sensitive to resolution. Given the similar entrainment behaviour of the B-scalar, the reason for the mean profile sensitivity to resolution shown in Figure 10 is clear. A similar but less direct correlation can be seen for θ in KPRO.

The error in u_*^2 is the smallest and shows little variation with resolution. As noted earlier in Section 6.5, the surface momentum flux in the models is constrained to be nearly that of the LES. The entrainment flux of momentum does vary, but its influence in these runs is substantially less than that of the surface flux or the horizontal pressure gradient. This leads to a rather well behaved surface flux.

MIX does a good job of predicting all but θ entrainment flux, showing the worst performance due to large $\Delta\theta$ and the subsequent over-entrainment of temperature as noted earlier.

7. Conclusions

Motions in the planetary boundary layer range widely in scale and can be associated with distinctly different mechanisms of transport. The challenge in PBL modelling is to find closures that effectively represent this turbulent transport while using finite computational resources. There are two methods by which modelers attempt to accomplish this task. The first is the representation of the essential characteristics of planetary boundary-layer flow in simplified models, a number of which have been presented here. The second is using the models at resolutions that result in low computational cost. This aspect of the approximation is also represented in

this study. Results presented here show that these two aspects of the modelling process are not entirely independent; at higher resolutions, the choice of physical parameterization is less important than the resolution at which the model is used. This is not the case at lower resolutions, where there are substantive differences in aggregate model performance both in mean profile and flux predictions.

One of the most important roles of any model is representing entrainment. In the comparison that has been presented here, it is clear that the different model formulations result in quite different behaviour near the entrainment zone, which is reflected in widely varying predictions of mean mixed-layer values. It has been shown that there can be significant errors produced by many of these formulations when compared the LES results. This is particularly true near the free convective limit for some models and in the weakly capped cases for other models where the model formulation is too simple to represent the local thermal and momentum distribution near the entrainment zone.

Having identified weakness in the ability of these models to predict entrainment, it seems useful to look for methods to improve them. It is likely that the performance of both local and non-local models can be significantly enhanced by including more realistic entrainment dynamics. This might be undertaken by tuning or fitting model structure and coefficients to LES data. A method having a better foundation would be the systematic examination of a number of high resolution LES runs designed to quantify the role of individual structures in entrainment. This could help define more clearly the functional relationship between the horizontally averaged mean state of the mixed layer and the rate of entrainment of overlying air. This effort should be coupled with observations from the entrainment zone which are just now becoming available (Mann *et al.*, 1995).

Aknowledegements

One of the authors (KWA) would like to thank the Atmospheric Environment Service of Canada for generous support to carry out this work. The National Center for Atmospheric Research is sponsored by the National Science Foundation.

A. Appendix: Detailed model descriptions

7.1. A.1. Mixed-layer model (MIX)

Within most of the convective PBL, mean values of wind speed, conserved thermodynamic quantities, and conserved scalar constituents are often found to be quite uniform in the vertical. This provides the basis for the mixed-layer model.

The values of the well-mixed variables are computed from the vertically integrated equations,

$$\frac{\partial U_m}{\partial t} = \frac{1}{z_i}(\langle u'w'\rangle_0 - \langle u'w'\rangle_i) + f(V_m - V_{gm}) \tag{39}$$

$$\frac{\partial V_m}{\partial t} = \frac{1}{z_i}(\langle v'w'\rangle_0 - \langle v'w'\rangle_i) + f(U_{gm} - U_m) \tag{40}$$

$$\frac{\partial \theta_m}{\partial t} = \frac{1}{z_i}(\langle w'\theta'\rangle_0 - \langle w'\theta'\rangle_i) \tag{41}$$

where z_i is the depth of the mixed layer, the subscript m represents a vertical average over the whole mixed layer, and subscripts 0 and i denote the surface and mixed-layer top, respectively. Solving of these equations requires knowing the surface and entrainment fluxes.

The surface fluxes are typically calculated from a PBL similarity formulation, and dependent on the mixed-layer mean and the surface values (see Deardorff, 1972b; Suarez *et al.*, 1983). The fluxes at the PBL top can be related to the time rate of change of the mixed-layer depth (i.e., the entrainment rate) and the jump of ϕ across the PBL top ($\Delta\phi$), by vertically integrating the governing equations across the PBL top, assumed of infinitesimal thickness:

$$-\langle w'\phi'\rangle_i = \Delta\phi \frac{\partial z_i}{\partial t}. \tag{42}$$

Here ϕ is any one of U, V, θ, B or C, and $\Delta\phi \equiv \phi^+ - \phi_m$ where ϕ^+ is the mean value of ϕ just above the PBL top. These step changes are computed from the following equations,

$$\frac{\partial \Delta\phi}{\partial t} = \frac{\partial \phi^+}{\partial z}\frac{\partial z_i}{\partial t} - \frac{1}{z_i}(\langle w'\phi'\rangle_0 - \langle w'\phi'\rangle_i), \tag{43}$$

with additional forcing terms $f(V - V_g)$ and $f(U_g - U)$ in the case of horizontal momentum. Thus, the only remaining unknown is the entrainment rate. Over the years, various closure formulations have been proposed for the entrainment rate, some were derived from the layer-mean turbulent-kinetic-energy (TKE) budget (see Ball, 1960) while others were based on the TKE budget at the inversion base (e.g., Tennekes 1973; Tennekes and Driedonks 1981).

In this study, we use the entrainment closure developed by Tennekes and Driedonks (1981) and Driedonks (1982), which is based on the governing equation for the TKE at the inversion base,

$$\frac{\partial e_i}{\partial t} = \frac{g}{\theta}\langle w'\theta'\rangle_i - [\langle u'w'\rangle_i \frac{\Delta U}{d} + \langle v'w'\rangle_i \frac{\Delta V}{d}] - [\frac{\partial}{\partial z}(\langle w'e'\rangle + \frac{\langle p'w'\rangle}{\rho})_i] - \epsilon_i \tag{44}$$

where d is an effective depth of the entrainment layer. The first term on the right hand side is buoyant production, the second shear production, followed by turbulent and pressure transports, and finally dissipation (Zeman and Tennekes, 1977). In order to solve this equation, each term in Equation (44) needs to be parameterized in terms of mixed layer mean values.

Although simpler parameterizations for the mixed-layer height can be arrived at by setting the left hand side of Equation (44) to zero, Zilitinkevich (1975) argued that when the mixed layer grows rapidly, this term cannot be neglected, and thus proposed

$$\frac{\partial e_i}{\partial t} = C_T \frac{w_t^2}{z_i} \frac{\partial z_i}{\partial t}. \tag{45}$$

Here the turbulent velocity scale (w_t) is an interpolation between the friction velocity (u_*) and the convective velocity (w_*),

$$w_t = (w_*^3 + 8.0u_*^3)^{1/3} \tag{46}$$

where the convective velocity is

$$w_* = [\frac{g z_i \langle w'\theta' \rangle_0}{\theta_m}]^{1/3} \tag{47}$$

in the unstable PBL. In the neutral PBL w_t simply scales with surface momentum flux,

$$w_t = 2.0u_* \tag{48}$$

after Zeman and Tennekes (1977).

Using Equation (42) and a scaling argument that $\frac{\Delta U}{d} \propto \frac{\Delta U}{z_i}$, the shear production in Equation (44) can be written as

$$-[\langle u'w' \rangle_i \frac{\Delta U}{d} + \langle v'w' \rangle_i \frac{\Delta V}{d}] = C_M \frac{(\Delta U)^2 + (\Delta V)^2}{z_i} \frac{\partial z_i}{\partial t}, \tag{49}$$

and after Tennekes (1973), the turbulent and pressure transport terms are parameterized as

$$-\frac{\partial}{\partial z}(\langle w'e' \rangle + \langle w'p' \rangle)_i = C_F \frac{w_t^3}{z_i}. \tag{50}$$

Although Tennekes and Driedonks (1981) point out that there is a substantial degree of arbitrariness in the choice of forms for the dissipation term, they choose

$$\epsilon_i = C_D w_t^2 N, \tag{51}$$

where N is the buoyancy frequency of the air just above the PBL,

$$N^2 = \frac{g}{\theta} \frac{\partial \theta^+}{\partial z}. \tag{52}$$

This leads to the entrainment closure we use in this study,

$$\frac{\partial z_i}{\partial t} = \frac{\frac{g}{\theta}\langle w'\theta'\rangle_i + C_F\frac{w_t^3}{z_i} - C_D w_t^2 N}{C_T\frac{w_t^2}{z_i} - C_M\frac{\Delta U^2+\Delta V^2}{z_i}} \tag{53}$$

where C_F, C_T, C_D and C_M are constants equaling 0.6, 4.3, 0.03 and 0.7, respectively.

A.2. STABILITY-BOUNDS MODEL (STAB)

In the model developed by Price *et al.* (1986), vertical mixing is accomplished by three mixing rules based on certain specified conditions for gravitational, mixed-layer entrainment, and shear (Kelvin-Helmholtz) stability. These conditions are neither demonstrably sufficient nor general from a theoretical point of view but have shown some empirical success at capturing mean profile behaviour for limited regimes. In this model the stability conditions are tested individually and in sequence. If a condition is violated, all fluid properties are mixed equally uniformly until the condition is satisfied within a time interval that is considered instantaneous. In this sense the mixing prescriptions are of the adjustment type.

The first condition is static stability,

$$\frac{\partial \rho}{\partial z} \leq 0 \tag{54}$$

where ρ is density and z is positive upward. The check for static stability is carried out after all the surface forcing, with the exception of the momentum flux, has been applied to the near surface grid level. The model column is completely mixed in all quantities from the surface to the interface below the first grid point that satisfies Equation (54). This interface is the first predicted mixed-layer depth, h_1, and any local gravitational instabilities beyond h_1 are unaffected by condition specified in Equation (54). This mixing is intended to simulate free convection, typically near the surface under strong heating conditions, but it cannot penetrate into stable stratification.

The second condition is for mixed-layer stability. The momentum flux is distributed uniformly from the surface to h_1, and a second mixed-layer depth, h_2 which is determined using a bulk Richardson number (see Pollard *et al.*, 1973; Price *et al.*, 1978):

$$R_b = \frac{g\Delta\rho h}{\rho_0(\Delta \mathbf{V})^2} \geq R_{bc} \equiv 0.65 \tag{55}$$

where Δ denotes the property difference between the mixed layer and the first layer beyond. Again, all properties are completely mixed from the surface to the interface below the first grid level that satisfies Equation 55; this interface then

defines h_2. This process is meant to represent deepening of the mixed layer by shear-driven entrainment.

Such entrainment generally leads to unrealistic property jumps across h_2 that are smoothed out by the parameterization of local shear (Kelvin-Helmholtz) instability. The associated condition,

$$R_g = \frac{g\partial\rho/\partial z}{\rho_0(\partial \mathbf{V}/\partial z)^2} \geq R_{gc} \equiv 0.25 \tag{56}$$

is applied across h_2 and everywhere beyond. This region is first searched for the smallest gradient Richardson number, R_g; then the two adjacent layers are partially mixed in all quantities according to

$$\phi_i = \phi_i + (\phi_{i+1} - \phi_i)\frac{1 - R_g/R_{new}}{2} \tag{57}$$

$$\phi_{i+1} = \phi_{i+1} + (\phi_i - \phi_{i+1})\frac{1 - R_g/R_{new}}{2} \tag{58}$$

where ϕ_i is the value in one layer and ϕ_{i+1} is the value in the other. We use a value of 0.3 for R_{new} following Price *et al.* (1986). Complete mixing occurs for $R_g = 0$, but since some local areas of gravitational instability could exist with $R_g < 0$, some excess mixing is possible. There is also a mixing discontinuity at $R_g = 0.25$, where the partial mixing in Equation (57) and Equation (58) equals 0.17, rather than zero. After this local mixing, new R_g values are computed where necessary and, in general, the procedure is repeated until Equation (56) is satisfied everywhere.

Finally the mixed-layer depth, h_m, is diagnosed from the resulting density profile. The local instability mixing can occur below h_2, which leads to $h_m < h_2$. In practice this mixing is arbitrarily confined to only the first two layers below, so Equation (56) may not be satisfied across h_m. It is also not necessary for Equation (55) to be satisfied for $h = h_m$.

A.3. $K(Ri)$ (LOUIS MODEL) (KOFR)

The $K(Ri)$ scheme is after Louis (1979), and incorporates the updates and changes in constants and formulations from Louis *et al.* (1981). The basis for the Louis model emerged from known behaviour of surface-layer turbulence, with Ri used as a similarity parameter instead of z/L. Louis made the coupling to the surface by a drag coefficient formulation whereas in the interior of the flow he switched to a traditional K-formulation.

Like the other grid-point models, the $K(Ri)$ model shares M-O similarity lower boundary condition for surface heat, momentum and scalar fluxes. Above the surface layer the fluxes are parameterized using Richardson number modified drag coefficients,

$$-\langle u'w'\rangle = a^2 U^2 F_m\left(\frac{z}{z_0}, Ri\right) \tag{59}$$

$$-\langle w'\theta'\rangle = \frac{a^2}{R} U \Delta\theta F_h \left(\frac{z}{z_0}, Ri\right) \tag{60}$$

where R is the ratio of drag coefficients for momentum and heat in the neutral limit, a^2 is the neutral momentum drag coefficient,

$$a = \frac{\kappa}{ln\left(\frac{z+z_0}{z_0}\right)} \tag{61}$$

and Ri is the Richardson number,

$$Ri = \frac{\frac{g}{\bar{\theta}}\frac{\partial\theta}{\partial z}}{\left(\frac{\partial|U|}{\partial z}\right)^2}. \tag{62}$$

Equations (59) and (60) can be recast in local form to give expressions for K_m and $K_h (\equiv K_\phi)$, the eddy diffusivities for momentum, heat and scalars above the surface layer,

$$K_{m,h} = l_{m,h}^2 \left(\frac{\partial U^2}{\partial z} + \frac{\partial V^2}{\partial z}\right)^{1/2} F_{m,h} \tag{63}$$

where,

$$l_{m,h} = \frac{\kappa z}{1 + \frac{\kappa z}{\lambda_{m,h}}}. \tag{64}$$

The asymptotic mixing lengths for momentum and heat, (λ_m and λ_h) are given values of 150 m and 450 m respectively.

Initially Louis used matching to surface-layer similarity functions to obtain F_m and F_h. These were later adjusted in the stable regime to provide a finite flux Richardson number in the limit of strong stratification. This is in agreement with empirical surface-layer similarity functions, so the model should be effective near the surface. Away from the surface the approach relies on the existence of a local relationship between fluxes and mean gradients, valid for arbitrary stratification. Although there is evidence for this in the stable case, boundary-layer diffusivities are not well behaved in the convective case. Furthermore, the stability functions obtained by Louis may not be consistent with turbulence behaviour in the mid- and outer regions of the stable boundary layer.

Louis *et al.* (1981) used the performance of the ECMWF forecast model in the upper troposphere to tune asymptotic mixing lengths λ_m and λ_h. Obtained values are thus also dependent on properties of the forecast model other than its ability to treat turbulent mixing. Comparisons with atmospheric turbulence data (Kim and Mahrt, 1992; Tjernström, 1993) have shown that the magnitudes of the asymptotic mixing lengths depend on the type of flow studied, with typically an order of magnitude smaller values obtained when tuned against data from boundary layers and thin shear layers.

After tuning and a number of modifications to the scheme Louis *et al.* (1981) give the following formulations for F_m and F_h in the unstable case,

$$F_m = 1.0 - \frac{2bRi}{1 + 2bc_m \frac{l_m^2}{\Delta z^{3/2} z^{1/2}} \left\{ \left(\frac{(z+\Delta z)}{z} \right)^{1/3} - 1 \right\}^{3/2} \mid Ri \mid^{1/2}}, \tag{65}$$

$$F_h = 1.0 - \frac{3bRi}{1 + 2bc_h \frac{l_h^2}{\Delta z^{3/2} z^{1/2}} \left\{ \left(\frac{(z+\Delta z)}{z} \right)^{1/3} - 1 \right\}^{3/2} \mid Ri \mid^{1/2}}. \tag{66}$$

For the stable and neutral cases, the following formulations for F_m and F_h are used,

$$F_m = \frac{1}{1 + \frac{2bRi}{(1+dRi)^{1/2}}}, \tag{67}$$

$$F_h = \frac{1}{1 + 3bRi(1 + dRi)^{1/2}}. \tag{68}$$

The constants used in the above closure equations are $\{b, c_m, c_h, d\} = \{5.0, 7.5, 5.0, 5.0\}$ (see Louis *et al.*, 1981).

A.4. K-PROFILE MODEL (KPRO)

Turbulent mixing in a large-scale atmospheric model is often treated by a first order, local diffusion approach, in which the subgrid-scale turbulent, vertical kinematic flux of a quantity is taken proportional to the local mean gradient of the transported quantity,

$$\overline{w'\phi'} = -K_\phi \frac{\partial \phi}{\partial z} \tag{69}$$

where ϕ is one of q, θ, u, v and K_ϕ is an "eddy-diffusivity" for ϕ, which is typically taken to be a function of a length scale and local vertical gradients of wind and potential temperature. This downgradient approach is a good approximation in the stable and neutral boundary layers, where mixing occurs on scales that are generally smaller than the depth of the boundary layer. In the convective boundary layer, the main mechanisms for transport of momentum, heat and scalars are buoyant plumes which scale with the depth of the mixed layer. Under these conditions, the downgradient diffusion approximation breaks down and transport can often be against the mean gradient or "countergradient" (Deardorff, 1972c). This is often the case near the top of the mixed layer where rising plumes encounter a capping inversion.

In the present evaluation of the non-local diffusion scheme, we follow the work by Troen and Mahrt (1986) while adopting the extensions of Holtslag and Boville (1993). By simplifying and approximating the heat and scalar flux equations (Holtslag and Moeng, 1991), the flux of any scalar ϕ can be described with

$$\overline{w'\phi'} = -K_\phi \left(\frac{\partial \phi}{\partial z} - \gamma_\phi \right). \tag{70}$$

Here K_ϕ is an eddy diffusivity for the quantity of interest, $\partial\phi/\partial z$ is the local gradient for ϕ, and γ_ϕ reflects the non-local transport due to dry convection. This formulation is non-local in two ways. The first is the countergradient term γ_ϕ which depends on the surface flux ($\langle w'\phi' \rangle_0$) and the depth of the mixed layer (z_i),

$$\gamma_\phi = a w_* \frac{\langle w'\phi' \rangle_0}{w_m^2 z_i} \tag{71}$$

where w_* and w_m are turbulent velocity scales to be described later. The second non-local aspect of the formulation is the fact that the local diffusivity K_ϕ is dependent upon the bulk characteristics of the mixed layer rather than simply local properties,

$$K_{m,t} = \kappa w_{m,t} z \left\{ 1 - \frac{z}{z_i} \right\}^2. \tag{72}$$

The velocity scale used for passive scalars is the same as that for temperature(w_t). Countergradient terms for momentum have not yet been used.

A.4.1. Turbulent Velocity Scales

In the surface layer, the turbulent velocity scale for scalars is

$$w_t = \frac{u_*}{\phi_h} \tag{73}$$

where, in the stable surface layer, following Dyer (1974) the dimensionless temperature gradient is

$$\phi_h = 1 + 5\frac{z}{L}, \quad 0 \le z/L \le 1.0 \tag{74}$$

$$\phi_h = 5 + \frac{z}{L}, \quad z/L > 1.0 \tag{75}$$

and L is the Obukhov length. The latter formulation provides a smooth match at $z/L = 1$ and prevents ϕ_h from becoming unrealistically large (or K_ϕ from becoming too small). In the unstable surface layer ϕ_h is

$$\phi_h = \left\{ 1 - 15\frac{z}{L} \right\}^{-1/2} \tag{76}$$

again after Dyer (1974).

The momentum velocity scale is formulated in a similar fashion. For the unstable case,

$$w_m = \frac{u_*}{\phi_m} \tag{77}$$

where ϕ_m is given by

$$\phi_m = \left\{1 - 15\frac{z}{L}\right\}^{-1/3} \tag{78}$$

while in the stable case, w_m and w_t are assumed to be equal (see Holtslag and Boville, 1993).

Above the surface layer, the velocity scales take on non-local formulations. The momentum turbulent velocity scale (w_m) is a weighted combination of u_* and the convective velocity,

$$w_m = (u_*^3 + c_1 w_*^3)^{1/3} \tag{79}$$

where c_1 is a constant and

$$w_* = ((g/\theta_0)\langle w'\theta'\rangle_0 z_i)^{1/3}. \tag{80}$$

The scalar turbulent velocity scale (w_t) is then found by scaling its momentum counterpart by the turbulent Prandtl number (Pr),

$$w_t = w_m/Pr. \tag{81}$$

The turbulent Prandtl number ($\equiv K_m/K_h = w_m/w_t$) is given by,

$$Pr = \frac{\phi_h}{\phi_m}\left(\frac{z}{L}\right) + a\kappa\frac{z}{z_i}\frac{w_*}{w_m} \tag{82}$$

where a is a constant. The constants a and c_1 are determined in the convective limit by matching Equations 70, 71 and 72 at the top of the surface layer ($z = 0.1z_i$).

A.4.2. Mixed-Layer-Depth Determination

The non-local structure of the mixed-layer diffusivities (K_m, K_h) as well as the countergradient term (γ_ϕ) are dependent upon the specification of the mixed-layer depth (z_i). Here we follow Troen and Mahrt (1986) and use and iterative method based on the bulk Richardson number formulated using the difference between the surface temperature and the temperature at the top of the mixed layer,

$$z_i = \frac{Ri_c(U_{z_i}^2 + V_{z_i}^2)}{g/\theta_s(\theta_{z_i} - \theta_s)}. \tag{83}$$

In this formulation it is assumed that parcels rise to some height of neutral buoyancy thus determining the vertical extent of mixing. The surface temperature (θ_s) is determined using similarity arguments and matching at the top of the surface layer,

$$\theta_s = \theta(z_s) + b\frac{\langle w'\theta'\rangle_0}{w_m} \tag{84}$$

where $\theta(z_s)$ is a near surface temperature determined using similarity theory and b is a constant determined using arguments similar to those for a and c_1.

A.5. SINGLE-POINT MODELS

One often used form of turbulence closure in boundary layer modelling is the second-order single-point closure model (Mellor and Yamada 1974; Launder *et al.* 1975; Zeman and Lumley 1976; Lumley 1978). In this type of closure, equations for the second moments are derived by applying Reynolds decomposition and averaging to the heat, momentum and scalar equations. The result is a set of differential equations for the second moments and the mean equations. Although the derivation of these equations is straightforward, a number of terms in the equations require parameterization, specifically third-order moments, pressure-strain correlations and dissipation terms. With suitable approximation for these terms a closed set of equations results.

The complexity of single-point closure is somewhat arbitrary in that, in principle, equations for turbulent moments of any order can be derived. Although models containing prognostic third-order moments have been used (André *et al.* 1978; Briere 1981; Moeng and Randall 1984), these are far from practical for use in large-scale models. Even at second order these models are typically too complex for inclusion in a large-scale model due to computational cost. Additionally, it is questionable if the advantage of using a more physically complete closure can be realized at vertical and horizontal resolutions similar to those of most large-scale models. For these reasons, most implementations of single-point closure in large-scale models are based on a truncation of the second-moment equations to some manageable form. One such method of hierarchical simplification is described in Mellor and Yamada (1974, 1982) in which the equations are simplified (truncated) based on an anisotropy scaling.

In this study we evaluate the Level 2 and 2.5 single-point models described in Mellor and Yamada (1982) and Yamada (1983). Eddy diffusivities in these models may be written

$$K_m = lqS_m \tag{85}$$

$$K_\phi = lqS_\phi \tag{86}$$

where ϕ is any scalar, and q is the square root of twice the turbulent kinetic energy. Here l is a turbulence "master length scale" for which we use the traditional Blackadar (1969) formulation,

$$l = l_0 \frac{\kappa z}{(\kappa z + l_0)}, \tag{87}$$

limited to a minimum value ($= 0.5q/N$), where N is the buoyancy frequency. In the above, l_0 is an asymptotic length scale derived from an integral of the turbulent kinetic energy,

$$l_0 = 0.20\frac{\int_0^\infty zqdz}{\int_0^\infty qdz}. \tag{88}$$

In the Level 2 version q is obtained from the diagnostic equation that follows when tendency and transport are neglected in the prognostic Level 2.5 equation for q. In the original model by Mellor and Yamada non-dimensional eddy diffusivities S_m and S_ϕ were different in Level 2 and Level 2.5 versions. Use of the Level 2.5 system can result, however, in non-realizable turbulence fields, as discussed by Mellor and Yamada (1982), and Helfand and Labraga (1988). Yamada (1983) circumvented this problem by simply using Level 2 S_m and S_ϕ also in the Level 2.5 model. In essence this means that the Level 2.5 model, as used here, is analogous to the E-l type models common in the engineering community. This may be appropriate for the vertical fluxes needed in a GCM, but casts some doubt on the fidelity of other second moments from the scheme.

Since the S_m and S_ϕ used here are, due to the above simplifications, diagnostic equations that depend only on the local gradient Richardson number, the Level 2 model is analogous to the Louis (1979) model. Following Yamada (1983) the values of S_m and S_ϕ are assumed to have lower limits given by the values obtained at a gradient Richardson number of 0.14. These artificial lower bounds on mixing are likely to have a non-negligible effect on the results.

Since our evaluation is done in terms of quasi-steady results, the tendency of turbulent kinetic energy in the Level 2.5 model should have only marginal effect on the results. The Level 2.5 model uses a downgradient-type closure for the turbulent transport of turbulent kinetic energy. It is well known that buoyancy effects are significant in third-moment budgets in the convective boundary layer. To what extent the neglect of this affects the results may be quantitatively examined only by inclusion of buoyancy in the parameterization of third moments. Common experience is however that the Level 2.5 model as a system provides reasonable results despite this deficiency.

A.5.1 The Level 2.5 Closure (MY25)

The version of the Level 2.5 model used in this study is after Yamada (1983),

$$K_m = lqS_m \tag{89}$$

$$K_\phi = lqS_m\alpha \tag{90}$$

where ϕ is any scalar including potential temperature.

$$S_m = 1.96\frac{(0.1912 - Ri_f)(0.2341 - Ri_f)}{(1 - Ri_f)(0.2231 - Ri_f)}, \quad Ri_f < 0.16 \tag{91}$$

$$S_m = 0.85, \quad Ri_f \geq 0.16 \tag{92}$$

$$\alpha = 1.318\frac{0.2231 - Ri_f}{0.2341 - Ri_f}, \quad Ri_f < 0.16 \tag{93}$$

$$\alpha = 1.12, \quad Ri_f \geq 0.16. \tag{94}$$

In this form of the closure, the flux Richardson number (Ri_f) is derived from the gradient Richardson number (Ri) using the following conversion,

$$Ri_f = 0.6588(Ri + 0.1776 - [Ri^2 - 0.3221Ri + 0.03156]^{1/2}), \quad Ri < Ri_c \tag{95}$$

$$Ri_f = Ri_{fc}, \quad Ri \geq Ri_c \tag{96}$$

where $Ri_{fc}(= 0.191)$ and $Ri_c(= 0.195)$ are critical flux and gradient Richardson numbers.

The turbulent kinetic energy is determined by the integration of a differential equation for twice the turbulent kinetic energy ($q^2 \equiv \langle u_i u_i \rangle$),

$$\frac{\partial q^2}{\partial t} = \frac{\partial}{\partial z}\left[lqS_q\frac{\partial q^2}{\partial z}\right] + 2(P_s + P_b + \epsilon) \tag{97}$$

where P_s is shear production,

$$P_s = -\langle u'w' \rangle \frac{\partial U}{\partial z} - \langle v'w' \rangle \frac{\partial V}{\partial z} \tag{98}$$

P_b is buoyancy production,

$$P_b = \frac{g}{\theta}\langle w'\theta' \rangle \tag{99}$$

and ϵ is the dissipation rate,

$$\epsilon = -\frac{q^3}{lB_1} \tag{100}$$

where B_1 ($\equiv 16.6$) and S_q ($\equiv 0.2$) are constants.

A.5.2. The Level 2 Closure (MY20)

The Level 2 model has a similar formulation for K_m and K_ϕ but differs in the assumption that production of turbulent kinetic energy is equal to its dissipation. This allows a simple algebraic formulation for q^2 rather than the solution of a differential equation. Using the above notation, the equilibrium value of q^2 is

$$q^2 = B_1 l^2 \left[\left(\frac{\partial U}{\partial z}\right)^2 + \left(\frac{\partial V}{\partial z}\right)^2\right](1 - Ri_f)S_m \tag{101}$$

where l is calculated from Equation (87).

A.6. MULTI-STREAM EXCHANGE MODEL (TRAN)

The multi-stream exchange model examined in this study is the transilient scheme (Stull 1984, 1993). It makes use of a "transilient" matrix which describes the material exchange between different cells within the mixed layer. That is,

$$\overline{S}_i(t+\Delta t) = \sum_{j=1}^{N} c_{ij}(t,\Delta t)\overline{S}_j(t) \tag{102}$$

where $\overline{S}_i$ is the state of a scalar and c_{ij} is the transilient matrix, the elements of which, after mixing, specify the fraction of air currently at level i which originated from level j (Stull, 1993). This method of mixing is predicated on the idea that mixing is advective rather than diffusive in nature and as such its description should encompass some form of non-local transport. In the transilient matrix, near-diagonal elements are associated with local mixing while off diagonal elements specify non-local mixing which can span the full depth of the mixed layer. Thus the scheme accommodates mixing due to eddies ranging in size from that of a grid volume to the depth of the mixed layer.

The transilient matrix is based on the mixing potential Y_{ij} between levels i and j in the column and makes use of a non-local turbulent kinetic energy equation:

$$Y_{ij} = \frac{\Delta t T_0}{(\Delta_{ij}z)^2}\left[(\Delta_{ij}U)^2 + (\Delta_{ij}V)^2 - \frac{g(\Delta_{ij}z)(\Delta_{ij}\theta)}{\theta R_c}\right] - \frac{D_Y \Delta t}{T_0} \tag{103}$$

where Δ_{ij} is a difference operator between variables at points i and j, $R_c(=0.21)$ is a critical Richardson number, T_0 (= 1000s) is a time constant, D_Y dissipation factor and $Y_{ij} = Y_{ji}$.

The matrix Y represents the "mixing potential". There are a number of modifications which Y undergoes before it is used to carry out mixing on the model variables. The first modification ensures that the elements of the matrix increase monotonically from the off-diagonal corners to the diagonal in both vertical and horizontal directions. This is accomplished by moving through the matrix, first by columns and then by rows from the off-diagonal corners toward the diagonal, and adjusting upward the matrix elements which are below the maximum of the previous column/row elements. The matrix diagonal elements are then set to the row maximum plus a reference mixing potential Y_{ref} (=1000) which represents subgrid scale local mixing.

$$Y_{ii} = max(Y_{i,i+1}, Y_{i,i-1}) + Y_{ref}. \tag{104}$$

The final step in producing the transilient matrix c_{ij} is to normalize the mixing potential matrix Y to satisfy continuity constraints. This is accomplished by multiplying the upper triangle of Y by the inverse of the maximum of the R_1 norms of the rows of Y. This is followed by the generation of a symmetric lower triangle

and the calculation of diagonal elements of c_{ij}. The diagonal elements (c_{ii}) are then set to 1.0 minus the sum of the *ith* row to ensure conservation of mass.

References

André, J.C., De Moore, G., Lacarrere, P., Therry, G., and Du Vachat, R.: 1978, 'modelling the 24 h Evolution of the Mean and Turbulent Structures of the Planetary Boundary Layer', *J. Atmos. Sci.* **35**, 1861–1883.

Andrén, A., Brown, A., Graf, J., Mason, P., Moeng, C-H., Nieuwstadt, F. T. M., and Schumann, U.: 1994, 'Large-Eddy Simulation of a Neutrally Stratified Boundary Layer: A Comparison of Four Computer Codes', *Quart. J. Roy. Meteorol. Soc.* **120**, 1457–1484.

Andrén, A. and Moeng, C-H.: 1993, 'Single-Point Closures in a Neutrally Stratified Boundary Layer', *J. Atmos. Sci* **50**, 3366–3379.

Andrén, A.: 1990, 'Evaluation of a Turbulence Closure Scheme Suitable for Air-Pollution Applications', *J. Appl. Meteorol.* **29**, 224–239.

Arya, S. P.: 1988, *Introduction to Micrometeorology*, Academic Press, 303 pp.

Augstein, H., Riehl, H. Ostopoff, F. and Wagner, V.: 1973, 'Mass and Energy Transports in an Undisturbed Atlantic Trade Wind Flow', *Mon. Wea. Rev.* **101**, 101–111.

Ball, F. K.: 1960, 'Control of Inversion Height by Surface Heating', *Quart. J. Roy. Meteorol. Soc.* **86**, 483–494.

Betts, A. K. and Miller, M. J.: 1986, 'A New Convective Adjustment Scheme. Part II: Single Column Tests using GATE Wave, BOMEX, ATEX and Arctic Air-Mass Data Sets', *Quart. J. Roy. Meteorol. Soc.* **112**, 693–709.

Bradshaw, P.: 1972, 'The Understanding and Prediction of Turbulent Flow', *Aero. J.* **76**, 403–418.

Briere, S.: 1981, 'Energetics of Daytime Sea-Breeze Circulation as Determined from a Two-Dimensional, Third-Order Turbulence Closure Model.', *J. Atmos. Sci.* **44**, 1455–1474.

Brost, R. A., Wyngaard, J. C., and Lenschow, D. H.: 1982, 'Marine Stratocumulus Layers. Part II: Turbulence Budgets', *J. Atmos. Sci.* **39**, 818–836.

Brown, R. C. and Foster, R. A.: 1994, 'On PBL Models for General Circulation Models', *Atmos. Ocean Syst.* **2**, 163–183.

Businger, J. A.: 1973, 'Turbulent Transfer in the Atmospheric Surface Layer', In D. A. Haugen (ed.), *Workshop on Micrometeorology*, Amer. Met. Soc, Boston, 392 pp.

Clarke, R. H., Dyer, A. J., Brook, R. R., Reid, D. G., and Troup, A. J.: 1971, 'The Wangara Experiment: Boundary Layer Data', *Tech. Paper 19, Div. Meteorol. Phys. CSIRO*, Australia.

Deardorff, J. W.: 1970, 'A Numerical Study of Three-Dimensional Turbulent Channel Flow at Large Reynolds Numbers', *J. Fluid. Mech.* **41**, 453–480.

Deardorff, J. W.: 1972a, 'Numerical Investigation of Neutral and Unstable Planetary Boundary Layers', *J. Atmos. Sci.* **29**, 91–115.

Deardorff, J. W.: 1972b, 'Parameterization of the Planetary Boundary Layer for use in General Circulation Models', *Mon. Wea. Rev.* **100**, 93–106.

Deardorff, J. W.: 1972c, 'Theoretical Expression for the Countergradient Vertical Heat Flux', *J. Geophys. Res.* **77**, 5900–5904.

Deardorff, J. W.: 1980, 'Stratocumulus-Capped Mixed Layers Derived from a Three-Dimensional model', *Bound. Layer Meteorol.* **18**, 495–527.

Driedonks, A. G. M.: 1982, 'Models and Observations of the Growth of the Atmospheric Boundary Layer', *Boundary-Layer Meteorol.* **23**, 283–306.

Dyer, A. J.: 1974, 'A Review of Flux-Profile Relations', *Boundary-Layer Meteorol.* **1**, 363–372.

Galperin, B. and Orszag, S. A. Eds.: 1993, *Large Eddy Simulation of Complex Engineering and Geophysical Flows*, Cambridge U. Press, 600 pp.

Garratt, J. R.: 1993, 'Sensitivity of Climate Simulations to Land-Surface and Atmospheric Boundary-Layer Treatment—A Review', *J. Climate* **6**, 419–449.

Grant, L. M.: 1986, 'Observations of Boundary Layer Structure Made During the 1981 KONTUR Experiment', *Quart. J. Roy. Meteorol. Soc.* **112**, 825–841.

Helfand, H. M. and Labraga, J. C.: 1988, 'Design of a Nonsingular Level 2.5 Second-Order Closure Model for the Prediction of Atmospheric Turbulence', *J. Atmos. Sci.* **45**, 113–132.

Herring, J. R. and Kerr, R. M.: 1982, 'Comparison of Direct Numerical Simulations with Predictions of Two-Point Closures for Isotropic Turbulence Convecting a Passive Scalar', *J. Fluid Mech.* **118**, 205–219.

Holland, J. Z. and Rasmusson, E. M.: 1973, 'Measurements of the Atmospheric Mass, Energy and Momentum Budgets over a 500 km Square of Tropical Ocean', *Mon. Wea. Rev.* **101**, 44–55.

Holtslag, A. A. M., De Bruijn, E. I. F., and Pan, H-L.: 1990, 'A High Resolution Air Mass Transformation Model for Short-Range Weather Forecasting', *Mon. Wea. Rev.* **118**, 1561–1575.

Holtslag, A. A. M. and Moeng, C-H.: 1991, 'Eddy Diffusivity and Countergradient Transport in the Convective Atmospheric Boundary Layer', *J. Atmos. Sci.* **48**, 1690–1698.

Holtslag, A. A. M. and Boville, B. A.: 1993, 'Local Versus Nonlocal Boundary-Layer Diffusion in a Global Climate Model', *J. Climate* **6**, 1825–1842.

Kerr, R. M.: 1985, 'Higher-Order Derivative Correlations and the Alignment of Small-Scale Structures in Isotropic Numerical Turbulence', *J. Fluid Mech.* **153**, 31–58.

Kim, J. and Mahrt, L.: 1992, 'Simple Formulation of Turbulent Mixing in the Stable Free Atmosphere and Nocturnal Boundary Layer', *Tellus* **44A**, 381–394.

Klemp, J. B. and Durran, D. R.: 1983, 'An Upper Boundary Condition Permitting Internal Gravity Wave Radiation in Numerical Mesoscale Models', *Mon. Wea. Rev.* **111**, 430–444.

Kline, S. J., Morkovin, M. V., Sovran, G., and Cockrell, D. J.: 1968, 'Methods, Predictions Evaluation and Flow Structure, Volume 1', *Proc. Computation of Turbulent Boundary Layers – 1968 AFOSR-IFP-Stanford Conference.*

Launder, B. E., Reece, G. T., and Rodi, W.: 1975, 'The Development of a Reynolds Stress Turbulent Closure', *J. Fluid. Mech.* **68**, 537–566.

Louis, J-F.: 1979, 'A Parametric Model of Vertical Eddy Fluxes in the Atmosphere', *Boundary-Layer Meteorol.* **17**, 187–202.

Louis, J-F., Tiedtke, M., and Geleyn, J-F.: 1981, 'A Short History of the PBL Parameterization at ECMWF', Workshop on Planetary Boundary Layer Parameterization, 25–27 November, 1981, ECMWF.

Lumley, J. L.: 1978, 'Computational modelling of Turbulent Flows', *Adv. Appl. Mech.* **18**, 123–176.

Mann, J., Davis, K. J., Lenschow, D. H., Oncley, S. P., Kiemle, C., Ehrt, G., Giez, A., and Schreiber, H. G.: 1995, 'Airborne Observations of the Boundary Layer Top, and Associated Gravity Waves and Boundary Layer Structure', Ninth Symposium on Meteorological Observations and Instrumentation, 27–31 March, 1995, American Meteorological Society, Boston, MA, pp. 113-116

McWilliams, J. C., Gallacher, P. C., Moeng, C-H. and Wyngaard, J. C.: 1993, 'modelling the Oceanic Planetary Boundary Layer', In B. Galperin and S. A. Orszag, (eds.), *Large Eddy Simulation of Complex Engineering and Geophysical Flows*, Cambridge U. Press, 600 pp.

Mellor, G. L. and Yamada, T.: 1974, 'A Hierarchy of Turbulence Closure Models for Planetary Boundary Layers', *J. Atmos. Sci.* **31**, 1791–1806.

Mellor, G. L. and Yamada, T.: 1982, 'Development of a Turbulence Closure Model for Geophysical Fluid Problems', *Rev. Geophys. Space Phys.* **20**(4), 851–875.

Moeng, C-H. and Schumann, U.: 1991, 'Composite Structure of Plumes in Stratus-Topped Boundary Layers', *J. Atmos. Sci.* **48**, 2280–2291.

Moeng, C-H. and Sullivan, P. P.: 1993, 'A Comparison of Shear and Buoyancy Driven Planetary-Boundary Flows', *J. Atmos. Sci.* **51**, 999–1022.

Moeng, C-H. and Wyngaard, J. C.: 1988, 'Spectral Analysis of Large-Eddy Simulations of the Convective Boundary Layer', *J. Atmos. Sci.* **45**, 3575–3587.

Moeng, C-H. and Wyngaard, J. C.: 1989, 'Evaluation of Turbulent Transport and Dissipation Closures in Second-Order modelling', *J. Atmos. Sci.* **46**, 2311–2330.

Moeng, C-H.: 1984, 'A Large-Eddy-Simulation Model for the Study of Planetary Boundary-Layer Turbulence', *J. Atmos. Sci.* **41**, 2052–2062.

Moeng, C-H. and Randall, D. A.: 1984, 'Problems in Simulating the Stratocumulus-Topped Boundary Layer with a Third-Order Closure Model', *J. Atmos. Sci.* **41**, 1588–1600.

Nieuwstadt, F. T. M., Mason, P. J., Moeng, C-H., and Schumann, U.: 1993, 'Large-Eddy Simulation of the Convective Boundary Layer: A Comparison of Four Computer Codes', In Durst *et al.* (eds.), *Turbulent Shear Flows 8*, Springer-Verlag, Berlin, 431 pp.

Pollard, R. T., Rhines, P. B., and Thompson, R. O. R. Y.: 1973, 'The Deepening of the Wind-Mixed Layer', *Geophys. Fluid Dyn.* **4**, 381–404.

Price, J. F. and Weller, R. A.: 1986, 'Diurnal Cycling: Observations and Models of the Upper Ocean Response to Diurnal Heating, Cooling and Wind Mixing', *J. Geophys. Res.* **91**(C7), 8411–8427.

Price, J. F., Mooers, C. N. K., and Van Leer, J. C.: 1978, 'Observation and Simulation of Storm-Induced Mixed Layer Deepening', *J. Phys. Oceanogr.* **8**, 582–599.

Randall, D. A., Shao, Q., and Moeng, C-H.: 1992, 'A Second-Order Bulk Boundary-Layer Model', *J. Atmos. Sci.* **49**, 1903–1923.

Rogallo, R. S. and Moin, P.: 1984, 'Numerical Simulation of Turbulent Flows', *Ann. Rev. Fluid Mech.* **16**, 99–137.

Schmidt, H. and Schumann, U.: 1989, 'Coherent Structure of the Convective Boundary Layer Derived from Large-Eddy Simulations', *J. Fluid Mech.* **200**, 511–562.

Smagorinski, J.: 1963, 'General circulation experiments with the primitive equations. I. The Basic Experiment', *Mon. Wea. Rev.* **91**, 99–164.

Stull, R. B.: 1993, 'Review of Non-Local Mixing in Turbulent Atmospheres: Transilient Turbulence Theory', *Boundary-Layer Meteorol.* **62**, 21–96.

Stull, R. B.: 1988, *An Introduction to Boundary Layer Meteorology*, Kluwer Academic Publishers, Boston, 666 pp.

Stull, R. B.: 1984, 'Transilient Turbulence Theory. Part 1. The Concept of Eddy Mixing Across Finite Distances', *J. Atmos. Sci.* **41**, 3351–3367.

Suarez, M. J., Arakawa, A., and Randal, D. A.: 1983, 'The Parameterization of the Planetary Boundary Layer in the UCLA General Circulation Model: Formulation and Results', *Mon. Wea. Rev.* **111**, 2224–2243.

Sullivan, P. P., McWilliams, J. C., and Moeng, C-H.: 1994, 'A Subgrid-Scale Model for Large-Eddy Simulation of Planetary Boundary-Layer Flows', *Boundary-Layer Meteorol.* **71**, 247–276.

Taylor, P. A. and Wyngaard, J. C.: 1990, *PBL Model Evaluation Workshop: European Centre for Medium-Range Forecasts, 14–15 August 1989, Reading*. World Climate Research Programme Series 42, WMO/TD 378.

Tennekes, H. and Driedonks, A. G. M.: 1981, 'Basic Entrainment Equations for the Atmospheric Boundary Layer', *Boundary-Layer Meteorol.* **20**, 515–531.

Tennekes, H.: 1973, 'A Model for the Dynamics of the Inversion above the Convective Boundary Layer', *J. Atmos. Sci.* **30**, 558–567.

Thompson, R. M., Payne, S. W., Reckel, E. E., and Reed, R. J.: 1979, 'Structure and Properties of Synoptic Scale Wave Disturbances in the Intertropical Convergence Zone of the Eastern Atlantic', *J. Atmos. Sci.* **36**, 53–72.

Tjernström, M.: 1993, 'Turbulence Length Scales in Stably Stratified Free Shear Flow Analyzed from Slant Aircraft Profiles', *J. App. Meteorol.* **32**, 948–963.

Troen, I. and Mahrt, L.: 1986, 'A Simple Model of the Atmospheric Boundary Layer: Sensitivity to Surface Evaporation', *Boundary-Layer Meteorol.* **37**, 129–148.

Wyngaard, J. C. Ed.: 1984, *Large-Eddy Simulation: Guidelines for its Application to Planetary Boundary Layer Research*. US Army Research Office Contract No. 0804.

Yamada, T.: 1983, 'Simulations of Nocturnal Drainage Flows by a q^2l Turbulence Closure Model', *J. Atmos. Sci.* **40**, 91–106.

Yamada, T. and Mellor, G. L.: 1979, 'A Numerical Simulation of BOMEX Data using a Turbulence Closure Model Coupled with Ensemble Cloud Relations', *Quart. J. Roy. Meteorol. Soc.* **105**, 915–944.

Zeman, O. and Lumley, J. L.: 1976, 'modelling Buoyancy Driven Mixed Layers', *J. Atmos. Sci.* **33**, 1974–1988.

Zeman, O. and Tennekes, H.: 1977, 'Parameterization of the Turbulent Kinetic Energy Budget at the Top of the Daytime Boundary Layer', *J. Atmos. Sci.* **34**, 111–123

Zilitinkevich, S. S.: 1975, 'Comments on a Paper by H. Tennekes', *J. Atmos. Sci.* **32**, 991–995.